

1 APOGEE 2: multi-layer machine- 2 learning model for the interpretable 3 prediction of mitochondrial missense 4 variants

5 Salvatore Daniele Bianco^{1,2}, Luca Parca^{1,3}, Francesco Petrizzelli¹, Tommaso Biagini¹, Agnese
6 Giovannetti⁴, Niccolò Liorni^{1,2}, Alessandro Napoli¹, Massimo Carella⁵, Vincent Procaccio^{6,7},
7 Marie Lott⁷, Shiping Zhang^{7,9}, Angelo Luigi Vescovi⁸, Douglas C. Wallace^{7,10}, Viviana Caputo²,
8 Tommaso Mazza^{1*}

9
10 ¹Bioinformatics Laboratory, Fondazione IRCCS Casa Sollievo della Sofferenza, S. Giovanni
11 Rotondo (FG), Italy

12 ²Department of Experimental Medicine, Sapienza University of Rome, Rome, Italy

13 ³Italian Space Agency, Rome, Italy

14 ⁴Clinical Genomics Unit, Fondazione IRCCS Casa Sollievo della Sofferenza, S. Giovanni
15 Rotondo (FG), Italy

16 ⁵Medical Genetics Laboratory, Fondazione IRCCS Casa Sollievo della Sofferenza, S. Giovanni
17 Rotondo, (FG) Italy

18 ⁶University of Angers, Genetics Department CHU Angers, Mitolab UMR CNRS 6015-INSERM
19 U1083, F-49000 Angers, France

20 ⁷Center for Mitochondrial and Epigenomic Medicine, The Children's Hospital of Philadelphia,
21 Philadelphia, Pennsylvania, USA

22 ⁸ISBReMIT Institute for Stem Cell Biology, Regenerative Medicine and Innovative Therapies,
23 Fondazione IRCCS Casa Sollievo della Sofferenza, San Giovanni Rotondo (FG), Italy.

24 ⁹Department of Biomedical and Health Informatics, The Children's Hospital of Philadelphia,
25 Philadelphia, Pennsylvania, USA

26 ¹⁰Department of Pediatrics, Division of Human Genetics, The Perelman School of Medicine,
27 University of Pennsylvania, Philadelphia, PA, USA

28
29 *corresponding author (E-mail: t.mazza@css-mendel.it, Tel: +39 06 44160526, Fax: +39 06
30 44160548)

31

32 ABSTRACT

33 APOGEE 2 is a mitochondrially-centered ensemble method designed to improve the accuracy
34 of pathogenicity predictions for interpreting missense mitochondrial variants. Built on the joint
35 consensus recommendations by the American College of Medical Genetics and
36 Genomics/Association for Molecular Pathology (ACMG/AMP), APOGEE 2 features an improved
37 machine learning method and a curated training set for enhanced performance metrics. It offers
38 region-wise assessments of genome fragility and mechanistic analyses of specific amino acids
39 that cause perceptible long-range effects on protein structure. With clinical and research use in
40 mind, APOGEE 2 scores and pathogenicity probabilities are precompiled and available in
41 MitImpact. APOGEE 2's ability to address challenges in interpreting mitochondrial missense
42 variants makes it an essential tool in the field of mitochondrial genetics.

43

44

45 **Keywords:** mitochondrial genomics; computational biology; pathogenicity prediction

46

47 Introduction

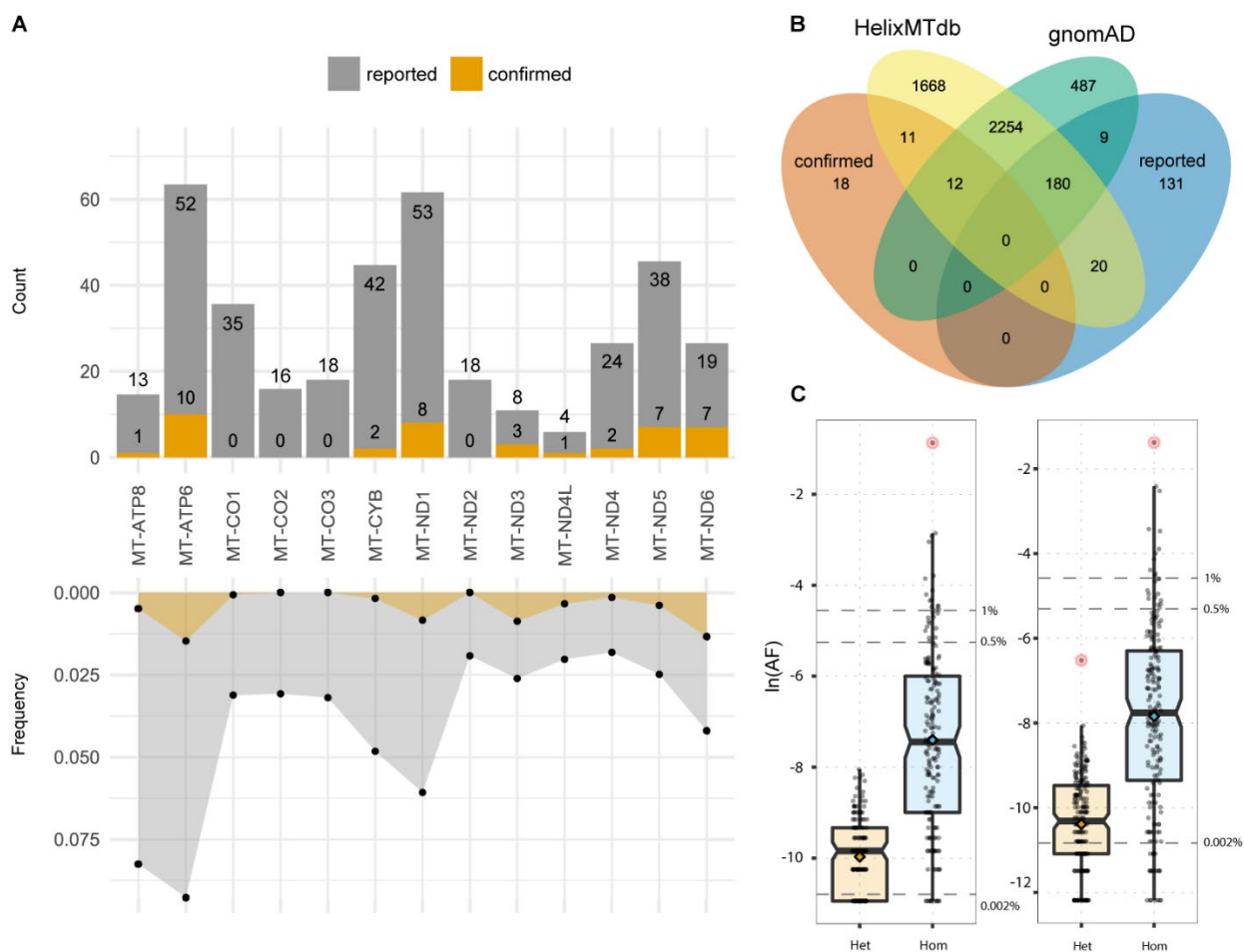
48 Mitochondria are responsible for many of the most important functions in eukaryotic cells. They
49 use oxidative phosphorylation (OXPHOS) to produce large amounts of adenosine triphosphate
50 (ATP), store calcium for cell signaling, generate heat, and mediate cell growth and death.

51 Mitochondria, in contrast to the nuclear genome (nDNA), have a smaller repertoire of DNA-
52 repair pathways. They counteract *Muller's ratchet*¹, the progressive accumulation of deleterious
53 mutations, with a process known as the *mtDNA bottleneck*, which, while controversial², explains
54 the increase in cell-to-cell variability in terms of mutant load during development. A unique
55 mechanism for the degradation of mutated DNA molecules³ eliminates defective cells, allowing
56 the mutant load to be stabilized over generations. Despite this, the mtDNA to nDNA variant
57 ratios range from a few folds in non-vertebrates up to at least 20 folds in vertebrates⁴. The lack
58 of protective histones in mitochondria, the proximity of mtDNA to the electron transport chain,
59 which is a primary cellular source of reactive oxygen species, or a dNTP pool imbalance that
60 leads to decreased DNA polymerase gamma fidelity⁵ are all factors that could affect these
61 ratios.

62 Mutations in the mtDNA are at the core of many human diseases⁶. Currently, ~1000 different
63 mutations are associated, based on literature, with human diseases in MITOMAP⁷, ~10% of
64 which with compelling evidence of being pathogenic based on published literature (named as
65 *confirmed* in MITOMAP), ~86% not been definitively shown to cause disease (named as
66 *reported*), and 4% including synergistic and conflicting variants. 94% of confirmed and reported
67 variants are single nucleotide variants (SNVs) and span the whole genome. Missense variants
68 account for 43% of all SNVs in MITOMAP (**Figure 1A**); 58% of them are present in the Genome
69 Aggregation Database (gnomAD)⁸ and 65% in HelixMTdb⁹ (**Figure 1B**).

70 As one might anticipate, the majority of gnomAD's missense variants are benign based on
71 ClinVar, but gnomAD also includes twelve MITOMAP confirmed missense variants and an

72 additional three that ClinVar classifies as pathogenic (**Supplementary Table 1**). In the case of
73 new variants or without a confirmed functional effect, one should apply the full 2020
74 ClinGen/ACMG/AMP guidelines ¹⁰. For allele frequency (AF), they allow an evidence weight of
75 “supporting” when a variant is found at an AF <1/50000 (<0.002%) in mitochondrial specific
76 databases (pathogenic criteria code “PM2”), “likely benign” when AF >0.5% (“BS1”), or “stand-
77 alone benign” when AF>1% and there is no other conflicting evidence, such as a novel
78 occurrence in a major haplogroup branch to support pathogenicity (“BA1”). While confirmed
79 variants are mostly rare ⁸, reported, conflicting, and synergistic variants are far more common.
80 Indeed, there are eight confirmed variants in gnomAD with AF \geq 0.002% (**Supplementary Table**
81 **1**) and 187 reported variants with AF \geq 0.002%, of which 28 with AF \geq 0.5% and 16 \geq 1%.
82 Similarly, HelixMTdb contains seven confirmed variants with frequencies \geq 0.002%
83 (**Supplementary Table 1**) and 191 reported variants \geq 0.002%, of which 23 have AF \geq 0.5% and
84 13 \geq 1% (**Figure 1C**). Because neither of the databases is enriched for mitochondrial disorders
85 or other clinical phenotypes, compared to the GenBank mtDNA sequence repository, these
86 variants are unlikely to be all pathogenic. As a result, the variant pathogenicity can be
87 challenging to predict as there are several biological mechanisms that concur with the functional
88 behavior, e.g., epistasis and modulatory effects, which cannot be solely based on allelic
89 frequency.



90

91 **Figure 1: A.** Counts (top) of reported and confirmed missense variants for all mtDNA protein-coding
92 genes and their frequency (bottom) calculated on each gene length. **B.** Common missense variants
93 between HelixMTdb, gnomAD, and MITOMAP's confirmed and reported variants. **C.** Distribution of
94 heteroplasmic (gnomAD, $n = 164$, HelixMTdb, $n = 204$) and homoplasmic (gnomAD, $n = 187$, HelixMTdb,
95 $n = 198$) reported variants in gnomAD (left) and HelixMTdb (right) based on their AF. Dashed lines
96 represent the 0.002%, 0.5%, and 1% AF thresholds. Error bars represent the 95% CIs around the median
97 values. Red dots are outlier variants by AF.
98

99 Inconsistencies were mitigated with the introduction of *in silico* prediction methods in 2015 by
100 the ACMG and AMP's joint consensus recommendations ¹¹, which were later implemented ¹⁰ for
101 the mitochondrial genome specifically. Variants were further given supporting evidence of
102 benign status ("BP4") when multiple lines of computational evidence suggested no impact on
103 the gene or gene product (coding non-synonymous variants: APOGEE score ≤ 0.5 ; tRNA
104 variants: MitoTip ¹² < 50 th percentile and HmtVar ¹³ < 0.35). On the contrary, variants were

105 assigned an evidence weight of supporting pathogenicity (“PP3”) when APOGEE >0.5; MitoTip
106 >50th percentile and HmtVar \geq 0.35.

107 The first version of APOGEE ¹⁴ was chosen over a slew of other options, the majority of which
108 were designed to work with nuclear-encoded genes. They had poor prediction records when
109 applied to mtDNA variants, evoking the historical congruency issue among predictors ¹⁵. As a
110 result, APOGEE was built as an ensemble method that was trained on mitochondrial-specific
111 features that contributed to the best classification performance among all competitors.

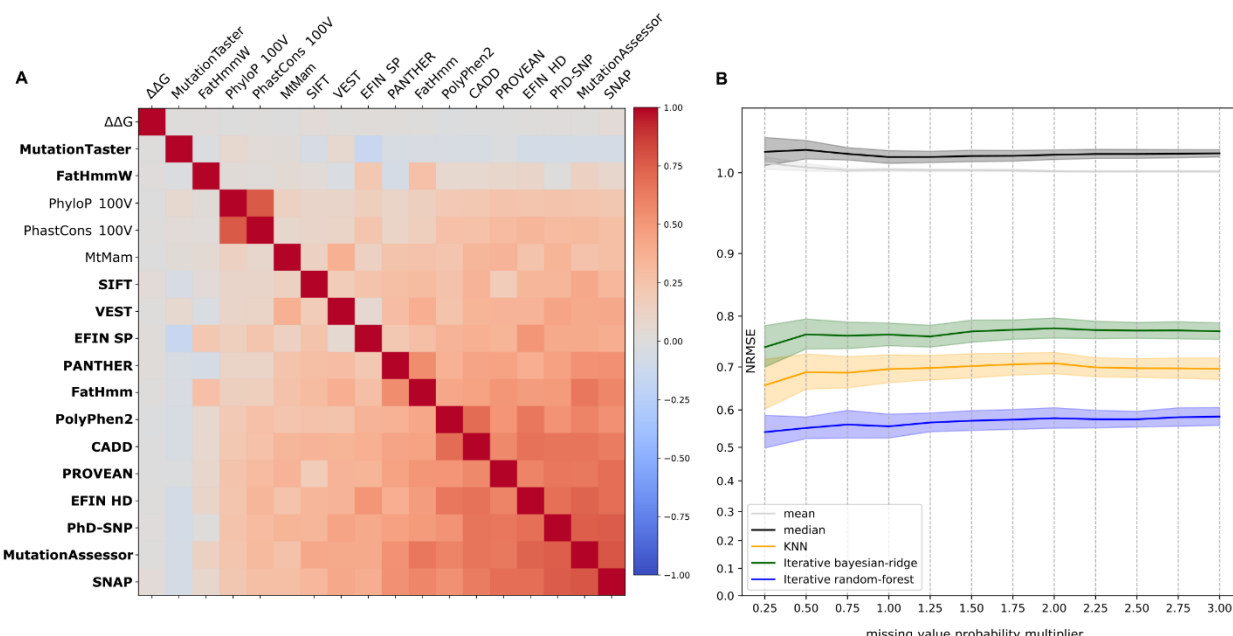
112 Here, we present its latest iteration. With a better, state-of-the-art, machine learning method and
113 a curated training set, APOGEE version 2 improves its own performance. We tested its ability to
114 spot pathogenic and neutral ¹⁶ variants in the mitochondrial genome and profiled its time-
115 dependent “learning curve” to demonstrate how the steadily growing number of high-quality
116 annotated mtDNA variants affects its classification performance. We have pre-calculated the
117 prediction scores and pathogenicity probabilities of all possible missense variants of the mtDNA
118 and set five classes of pathogenicity to support clinicians and geneticists in reporting their
119 genetic diagnoses. Finally, we have conducted a mechanistic analysis of specific amino acids
120 that cause perceptible long-range effects on the protein structure to discuss the significance of
121 strengthening protein structural features in the training set.

122 Results

123 Characteristics of the training set

124 The APOGEE 2 training set (**Dataset 1**) contains 140 pathogenic and likely harmful variants and
125 1734 benign and likely harmless variants that have been manually curated (see Methods for a
126 detailed description of the datasets). These were annotated with mitochondrially-tailored
127 evolutionary, positional, and structural features and fourteen pathogenicity assessments of *in*
128 *silico* predictors. Most of their Pearson correlation coefficients were in the range (-0.5, 0.5);

129 MutationAssessor, SNAP, and PhD-SNP exhibited absolute Pearson's r values >0.7 with more
130 than one other feature (**Supplementary Figure 1A** and **Supplementary Table 2**).
131 Features were not always available for all variants. Missing values accounted for 1% of the
132 evolutionary scores and *in silico* predictions and 0.2% of structural and positional values. We
133 imputed them by using a Random Forest-based iterative imputer, which displayed the lowest
134 Normalized Root Mean Squared Error (NRMSE) values of all tested imputation methods
135 (**Supplementary Figure 1B**).



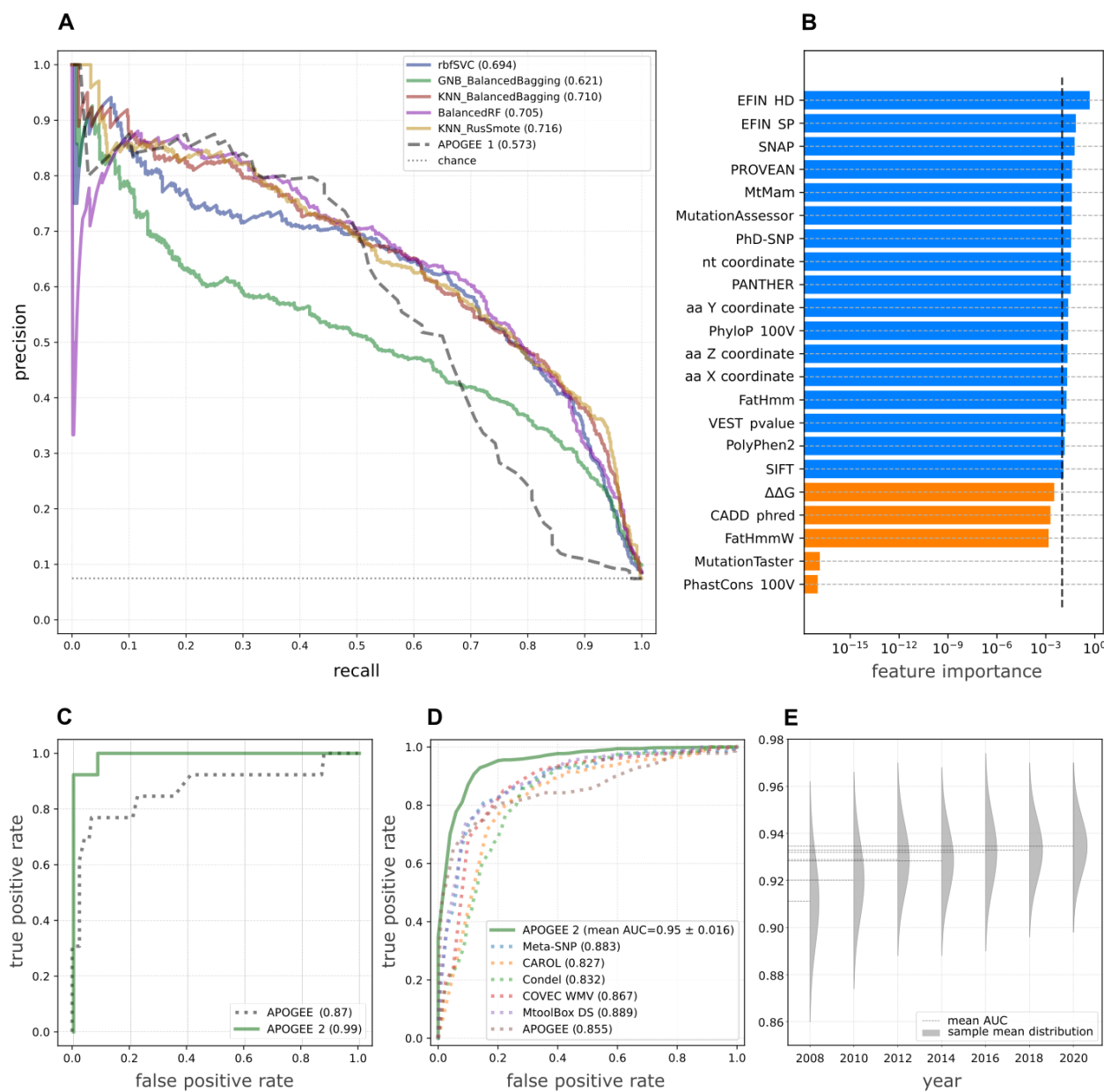
136
137 **Supplementary Figure 1: A.** Matrix of Pearson correlation coefficients calculated on the scaled
138 prediction scores to zero mean and unit variance of non-positional features for all possible mitochondrial
139 missense variants. Axes labels related to pathogenicity predictors are highlighted in bold. **B.** Imputation of
140 missing values with five algorithmic strategies; performance is measured in terms of Normalized Root
141 Mean Squared Error (NRMSE, Y-axis); multipliers of the *a priori* probability of missing values in MitImpact
142 (i.e., the unitary value) on the X axis (see Methods); both mean errors (lines) and their 95% CI (colored
143 shadows) are reported in the figure.
144

145 Training, testing, and performance assessment

146 We examined different machine-learning (ML) classification methods to sort deleterious
147 variants, searching for the best-performing one, while all were designed to properly tackle the

148 class imbalance in **Dataset 1**. Each method was instantiated during a 20-fold cross-validation
149 (CV) repeated five times, where 19 folds of the dataset were iteratively used for the training and
150 tuning of the hyperparameters, and the remaining fold was used for testing. Each method was
151 tuned by attempting several combinations of hyperparameters (**Supplementary Table 3**). This
152 was done using an inner 10-fold Grid-Search (GS) CV.
153 With the highest average test auPRC (0.716, **Figure 2A**), auROC (0.95), and the best records
154 for nearly all performance metrics (**Supplementary Table 4**), the KNN Bagging balanced
155 through Random Under-Sampling (RUS) and Synthetic Minority Oversampling Technique
156 (SMOTE) method (KNN_RusSmote) stood out as the best and was then chosen as the
157 APOGEE 2 ML reference method. The best hyperparameters identified by GS were: "3" for the
158 number of KNN's *neighbors*; the inverse euclidean distance as a metric to weight the neighbors'
159 importance; 1/4 as the pathogenic/neutral variant ratio before the SMOTE step; and 1/4 as the
160 ratio of features used by each base learner over the total number of selected features. It used
161 17 out of the 22 considered features, where PhastCons 100V, MutationTaster, FatHmmW,
162 CADD, and $\Delta\Delta G$ were, in fact, discarded in the feature selection step (**Figure 2B**).
163 On **Dataset 1**, APOGEE version 1 underwent a second round of testing and received an
164 average auPRC of 0.573 (**Figure 2A**) and auROC of 0.855. The classification performance of
165 both APOGEE versions was also compared on the test set of our previous work ¹⁵, which
166 included the union of MITOMAP and VariBench variants available at the time of that writing (see
167 Supplementary Table 2 in ¹⁵) purged of variants overlapping with the APOGEE 2 training.
168 APOGEE 2 outperformed its former version (0.99 vs. 0.87 auROC, **Figure 2C**; 0.97 vs. 0.65
169 auPRC).
170 Compared with other meta-predictors, APOGEE 2 exhibited the best performance metrics,
171 including auPRC (**Figure 2D**), but the sensitivity where MtoolBox and Condel excel at the
172 expense of specificity, which ranked worst for both tools (**Supplementary Table 4**).

173 To evaluate whether expanding APOGEE 2's training set would improve its performance in
174 future releases, we adopted the same criteria used to create **Dataset 1** to generate seven
175 training sets starting from the MITOMAP content from 2008 to 2020, which was randomly
176 retrieved once every two years. The 2022 content was used as a test set. We found that the
177 models' performance in sorting pathogenic from neutral variants in the 2022 dataset increased
178 monotonically over time (Pearson's r : 0.91, p -value: 0.004), but at an increasingly slower rate
179 (**Figure 2E, Supplementary Table 10**), indicating that expanding the training set in subsequent
180 iterations will not have as much of an impact on APOGEE 2's performance as adding more
181 informative features would.



182

183 **Figure 2: A.** Average test auPRC values of the selected ML methods, calculated during the training
 184 phase. Support Vector Machine classifier with radial basis functions kernel (rbfSVC), Balanced Bagging
 185 using Gaussian Naive Bayes (GNB_BalancedBagging) and K-Nearest Neighbors
 186 (KNN_BalancedBagging) as base estimators, Balanced Random Forest (BalancedRF), KNN Bagging
 187 balanced through RUS and SMOTE techniques (KNN_RusSmote). **B.** Feature importance assessed on
 188 the whole Dataset 1; threshold set to 1%. **C.** AuROC values calculated on 118 and 13 neutral and
 189 pathogenic test variants for APOGEE versions 1 and 2. **D.** Performance comparison of APOGEE 2 versus
 190 other meta-predictors in terms of auROC. APOGEE 2's auROC is reported as the mean \pm 95% CIs
 191 obtained through cross-validation. **E.** Time-dependent APOGEE 2's auROC values obtained by predicting
 192 MITOMAP 2022 upon training on the 2008-2020 contents; for each year, the sample mean distribution is
 193 reported in gray.
 194

195 **Whole-genome predictions**

196 We used APOGEE 2 to predict the pathogenicity of all 24190 possible missense mtDNA
197 variants (**Supplementary Table 5**) and made them available in MitImpact.

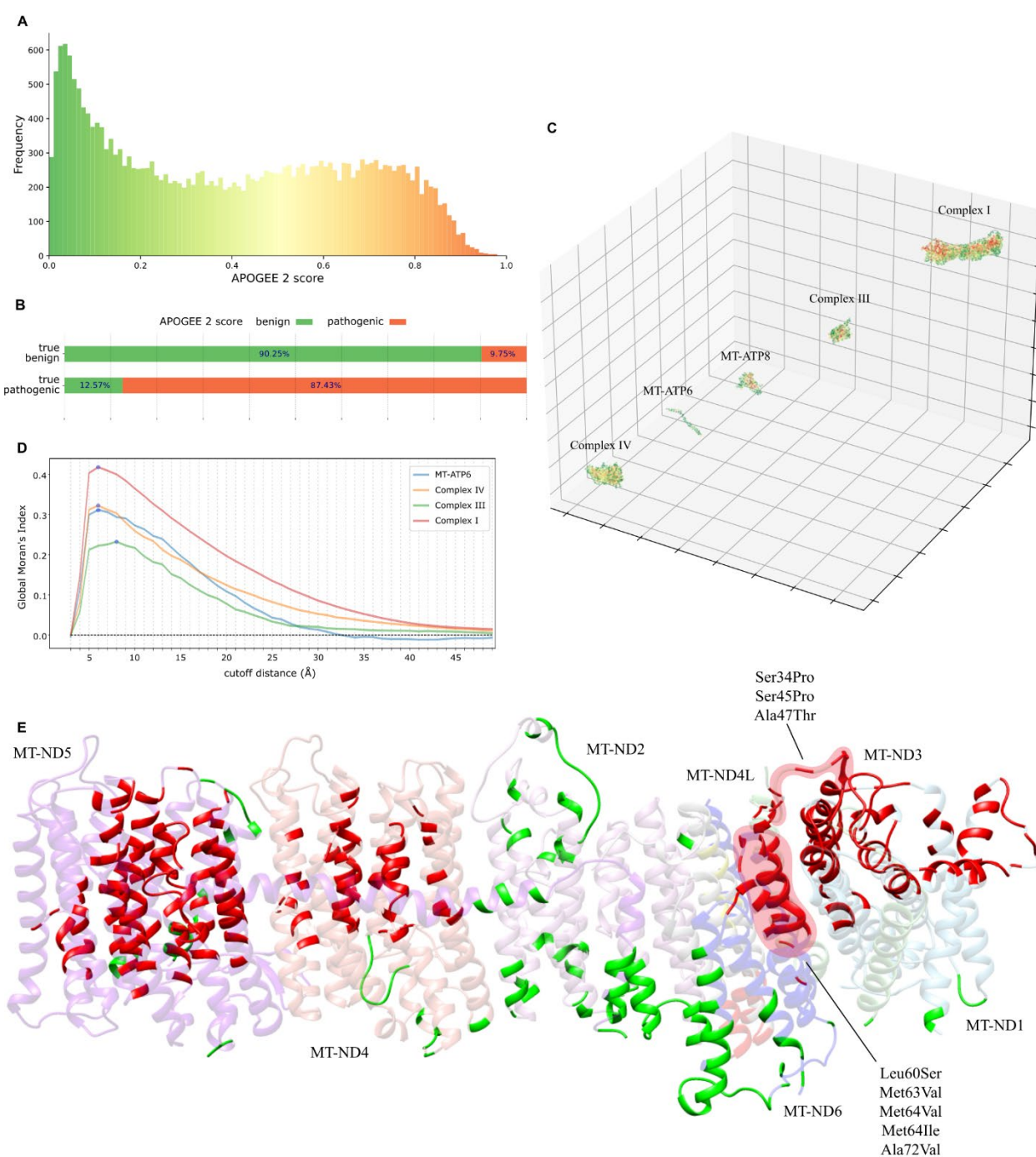
198 **Scores and pathogenicity probabilities.** Prediction scores are numeric and do not follow a
199 conventional probability density function. The exact frequency distribution is shown in **Figure**
200 **3A.** Scores range from 0 (neutral or benign) to 1 (deleterious or pathogenic). Using Bayesian
201 reasoning, we could determine the posterior pathogenicity probability associated with all
202 missense mitochondrial variants, ranging from 0 (not pathogenic) to 1 (pathogenic). Since the
203 posterior probability monotonically increases with the APOGEE 2 score, ranking variants by one
204 metric or the other is equivalent.

205 **Misclassification.** The misclassification analysis calculated for any of the 100 test folds
206 revealed that 12.57% of the pathogenic variants were deemed benign, while 9.75% of the
207 neutral variants were misclassified as deleterious (**Figure 3B**).

208 **Positionality.** The dependency of the APOGEE 2 score on the variants' locations in the
209 protein's 3D structures placed on a bisector of a 3D space (**Figure 3C**) was quantified using
210 Moran's index. For this analysis, we recalculated the APOGEE 2 scores by excluding the spatial
211 features from the learning workflow in order to avoid any positional bias. We found significant
212 positive spatial autocorrelation among the predicted pathogenic variants in each mitochondrial
213 complex (Moran's index permutation p-value <10E-5 for each complex except MT-ATP8, for
214 which p-value =0.02), implying that some regions of these proteins may be less tolerant to
215 amino acid changes than others. We performed this analysis with the quadratic distance decay
216 function as a measure of the proximity between amino acids. We also repeated the test using
217 binary proximity matrices, computed at different cutoff distances as described in ¹⁸. The
218 maximum Moran's index has been obtained when setting a cutoff distance between amino acids
219 of 6Å for Complex I, Complex IV, and MT-ATP6, and 8Å for Complex III (**Figure 3D**); no
220 significant results were obtained for MT-ATP8.

221 We localized spatially autocorrelated high- and low-risk regions using the LISA index. The most
222 significant regions (adjusted LISA permutation p-value <0.01) were reported in **Supplementary**
223 **Table 6**. The APOGEE 2 score threshold used to sort low- from high-risk amino acids in this
224 analytical step was 0.379, which is the median recalculated APOGEE 2 score. For example,
225 focusing on Complex I, which is composed of seven mtDNA-encoded proteins, we identified
226 several neutral hotspots spread throughout MT-ND2 and several fragile regions, which included
227 the transmembrane helices of MT-ND5, MT-ND4 and MT-ND1, the transmembrane helix 3
228 (TMH3) of MT-ND6 and the MT-ND3 loop. The latter two regions include variants known to
229 impact important physiological mechanisms, which were examined more deeply in the
230 “*Evaluation of variants that alter the protein structure non-locally*” section (**Figure 3E**).
231 **Categorization.** Interpreting the evidence categories given in Tables 3 and 4 of ¹¹ as
232 categorical conditional probabilities or odds of pathogenicity, in line with ¹⁷, and aiming to
233 provide clinical translationality to APOGEE 2 predictions, we adopted the following ranges of
234 probability and set four classes of pathogenicity: benign ≤ 0.001, 0.001 < likely benign ≤ 0.1, 0.9
235 ≤ likely pathogenic < 0.99, pathogenic ≥ 0.99. When none of the previous criteria are met, i.e.,
236 when the posterior pathogenicity probability of a variant is between 0.1 and 0.9, a variant has
237 uncertain significance (VUS) (**Supplementary Table 5**). With this setting, all known pathogenic
238 variants in **Dataset 1** were correctly labeled pathogenic and likely-pathogenic, except for seven
239 of them, which were annotated as VUS. Regarding the harmless variants in **Dataset 1**, 190
240 were annotated as VUS, while the remaining 1544 were correctly labeled benign and likely-
241 benign (**Supplementary Table 5**). Nearly all variants in **Datasets 2** and **3**, which contain only
242 potentially harmless variants and therefore were used to evaluate APOGEE 2’s specificity, were
243 classified as benign or likely-benign by APOGEE 2 (**Supplementary Table 7**: $\chi^2(1, N=36) =$
244 16.19, $p = 5.73E-05$ and $\chi^2(1, N=35) = 24.10$, $p = 9.15E-07$, respectively for **Datasets 2** and **3**).
245 None of the variants in **Dataset 2** were classified as pathogenic or likely-pathogenic, while one
246 variant from **Dataset 3** was classified as likely-pathogenic.

247



248

249 **Figure 3: A.** Distribution of APOGEE 2 scores. Colors represent classes of pathogenicity: green (benign, 250 probability of pathogenicity (P) ≤ 0.001), light green (likely benign, $0.001 < P \leq 0.1$), yellow (VUS, $0.1 < P < 0.9$), 251 orange (likely pathogenic, $0.9 \leq P < 0.99$), red (pathogenic, $P \geq 0.99$). **B.** Misclassification rate of 252 100 test folds calculated on Dataset 1. **C.** Mitochondrial protein complexes localization on the bisector of 253 a 3D space. Colors have the same meaning as **Figure 3A**. **D.** Global spatial autocorrelation computed at 254 different cutoff distances. Blue circles mark the maximum values for each protein complex. **E.** Low-risk 255 (green) and high-risk (in red) amino acid regions of the mitochondrial Complex I subunits. Highlighted in

256 red, we underline the MITOMAP confirmed variants that localize on TMH3 of MT-ND6 and on the MT-
257 ND3 loop.
258

259 Variant functionality prediction in human variation databases

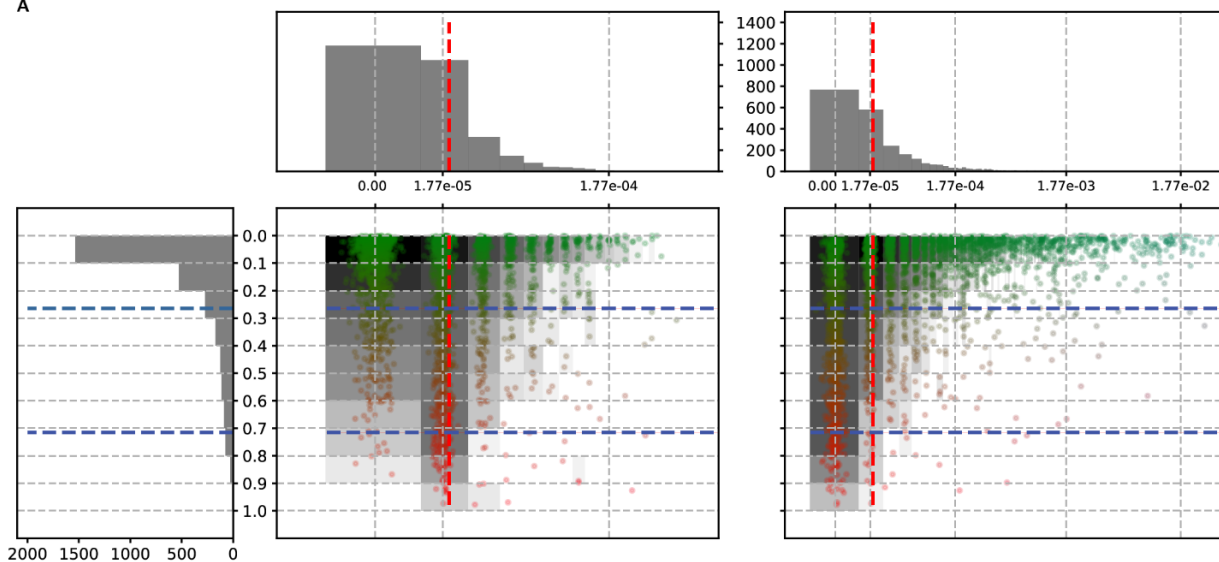
260 As a further test of the negative variants, we used APOGEE 2 to score every mitochondrial
261 missense variant in the gnomAD v3.1.2 and HelixMTdb databases. Heteroplasmic variants were
262 1767 (AF range min 0.0017%: max 0.037%) in gnomAD and 3058 (AF range min 0.0005%: max
263 0.15%) in HelixMTdb. The homoplasmic variants were 2177 (AF range min 0.0017%: max 99%)
264 and 2894 (AF range min 0.0005%: max 99%). The predicted pathogenic and likely pathogenic
265 variants for both databases were comparable (**Supplementary Figure 2A,B**), even when
266 considering <0.002% variants, irrespective of their heteroplasmy levels. GnomAD and
267 HelixMTdb showed, in fact, a high and significant positive correlation between the allelic
268 frequencies of their heteroplasmic (Pearson's r : 0.88, p-value <2.2E-16) and homoplasmic
269 (Pearson's r : 0.91, p-value =6.434E-11) variants.

270 It is important to note that HelixMTdb was not enriched in patients with mitochondrial diseases,
271 but there were no exclusion criteria based on mitochondrial disorders ⁹. On the other hand,
272 while gnomAD declares that some individuals with severe disease may still be included in the
273 database, albeit likely at a frequency equivalent to or lower than that seen in the general
274 population, they have explicitly removed individuals known to be affected by severe pediatric
275 disease, as well as their first-degree relatives. This might explain the presence of both likely and
276 frankly pathogenic variants in both datasets.

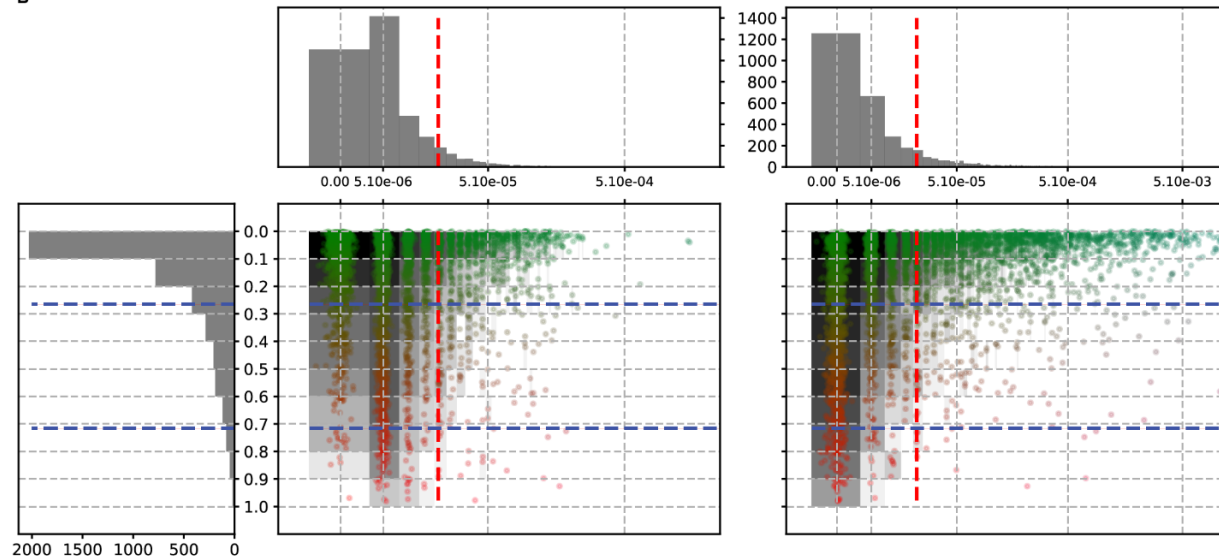
277 The pathogenicity probability values for ClinGen's neutral variants, which were collected in
278 **Dataset 4 (Supplementary Table 7)**, ranged from 0 to 0.73. **Dataset 4** (see Methods) contains
279 neutral variants that were evaluated by the ClinGen mitochondrial VCEP team and, therefore,
280 are supposedly more likely to be neutral than those contained in **Datasets 2 and 3**. None of
281 **Dataset 4** variants was predicted as pathogenic or likely-pathogenic by APOGEE 2. We also

282 verified that the APOGEE 2 scores of these variants were lower on average than those of the
283 neutral variants in **Dataset 1** (Mann-Whitney U test, $U=152940$, $p\text{-value}=2.80\text{E-}09$;
284 **Supplementary Figure 2C**), thereby confirming the ability of APOGEE 2 to also quantify the
285 level of certainty of being a neutral variant.

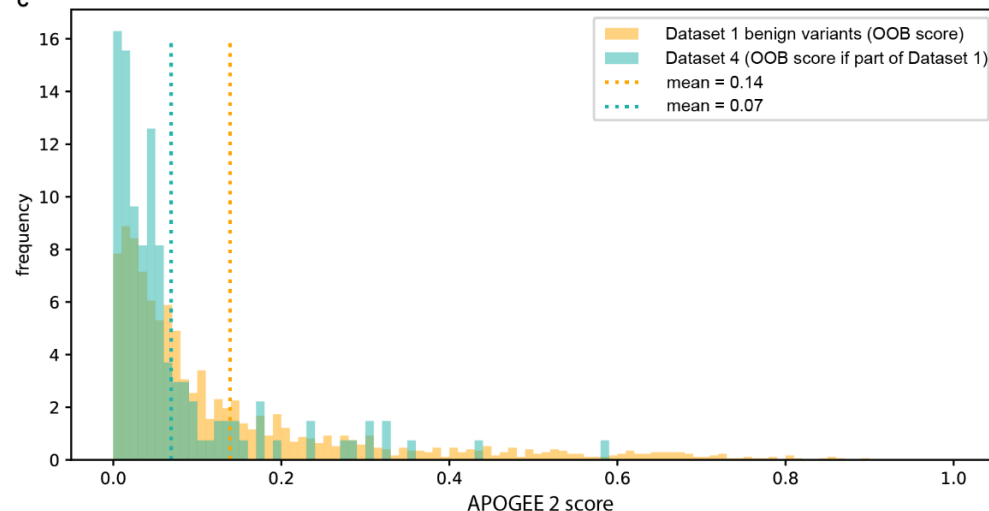
A



B



C



287 **Supplementary Figure 2: A.** 83 (4.7%) heteroplasmic variants in gnomAD were predicted to be likely
288 pathogenic, and 10 (0.6%) were pathogenic. 71 (4%) and 7 (0.4%) variants exhibited an AF <0.002%,
289 respectively. 19 (0.9%) homoplasmic variants were classified as likely pathogenic and 3 (0.1%) as
290 pathogenic. 11 (0.5%) and 1 (0.05%) variants exhibited an AF <0.002 %, respectively. **B.** 101 (3.3%)
291 HelixMTdb heteroplasmic variants were predicted as likely pathogenic, and 15 (0.5%) were classified as
292 pathogenic. Similarly, 33 (1.1%) homoplasmic variants were defined as likely pathogenic, and 3 (0.1%)
293 were deemed pathogenic. 86 (2.8%) heteroplasmic and 22 (0.8%) homoplasmic likely pathogenic
294 variants exhibited an AF <0.002%; 13 (0.4%) and 2 (0.07%) considering heteroplasmic and homoplasmic
295 pathogenic variants, respectively. Both panels represent the APOGEE 2 pathogenicity probability values
296 of heteroplasmic (left) and homoplasmic (right) variants on the Y axis and the variant AF on the X axis. A
297 dot is a variant. A dot color represents the pathogenicity level (green = benign, red = pathogenic), as in
298 Figure 3D. The red dashed line marks the 0.002% AF threshold. The blue dashed lines separate likely-
299 benign from VUS (score = 0.2654, probability = 0.1) and VUS from likely-pathogenic (score = 0.7161,
300 probability = 0.9). **C.** Frequency distribution of APOGEE 2 scores of Dataset 1's benign variants (training
301 set) and Dataset 4's variants (ClinGen). Vertical dashed lines mark the average APOGEE 2 scores for
302 both distributions.
303

304 **Evaluation of variants that alter the protein structure non-locally**
305 Variants that have structural and non-local effects may significantly impair APOGEE 2 prediction
306 performance. This is the case of NC_012920.1:m.10161A>C ¹⁹, (YP_003024033.1:p.Thr35Pro)
307 which is located in the MT-ND3 loop (residues 24 to 54) and is contiguous to the m.10158T>C
308 (p.Ser34Pro) common variant, reported as “confirmed” by MITOMAP, as “pathogenic” in
309 ClinGen, and is associated with Leigh disease or MELAS syndrome. The loop is between two
310 transmembrane helices (TMH 1 and 2) and includes Cys39. In mammalian Complex I, such a
311 residue is exposed during active mitochondrial respiration and is thought to be necessary for the
312 reversible transition between catalytically active and inactive states ¹⁹. Intuitively, the loop's
313 dynamics may influence Cys39 exposure and, as a result, the active-inactive state transition.
314 Multiple MD simulations revealed that the Ser34Pro and Thr35Pro mutants affect the loop
315 flexibility significantly and similarly to the wild-type protein, and the other two mutant systems,
316 Ser34Phe and Ser34Tyr (**Figure 4A-D**), which were chosen because of their allelic frequencies
317 (0.013% and 0.002% in MITOMAP, respectively), were contiguous and not associated with any
318 relevant phenotype. The RMSF profiles (**Figure 4C**) of the heavy atoms in part of the loop
319 (residues 40 to 50) were higher for Ser34Pro and Thr35Pro than the wild-type and slightly more
320 rigid in the first part (residues 24 to 40). On the other hand, Ser34Phe and Ser34Tyr displayed

321 flexibility profiles that were similar to those of the wild-type. This can also be observed in the 3D
322 dynamic representation (**Figure 4D**). The loss of essential interactions between loop residues
323 and nearby subunits brought on by Thr35Pro, such as residues 129 of MT-ND1 and 49 of MT-
324 ND3 and residues 76 of MT-ND6 and 48 of MT-ND3, is what leads to the flexibility alterations.
325 APOGEE 2 classifies this variant as VUS (score 0.51, probability = 0.59) even though we have
326 confirmed it to be pathogenic [Milon et al., under review].

327 A second case regards NC_012920.1:m.14538A>G, YP_003024037.1:p.Phe46Leu in MT-ND6,
328 reported in the literature ²⁰ as a novel pathogenic LHON variant but classified as likely-benign by
329 APOGEE 2 (score 0.08, probability = 0.002). It is proximal to the transmembrane helix TMH3
330 (residues 52–74 in the closed state and interrupted by a bulge in the open state that involves
331 residues 60–65 ²¹ of MT-ND6, which actively participates in the Complex I closed conformation,
332 rotating to lose its characteristic π -bulge and consequently disrupting the helix ²². A few
333 pathogenic mutations were found in the helix. One of them, m.14459G>A, hits the residue
334 Ala72, reported in MITOMAP and ClinGen as a pathogenic change in *valine* and associated
335 with multiple mitochondrial phenotypes. It is interesting to note that the same residue is also hit
336 by a proline variant (Ala72Pro, m.14460C>G). The proline variant is included in **Dataset 1**
337 because it is deemed benign due to its allelic frequency of 0.011%, but it is categorized as VUS
338 by APOGEE 2 (score = 0.64, probability = 0.82). We have compared the long-range impact of
339 p.Phe46Leu on TMH3 with that caused by Ala72Pro and Ala72Val by simulation. After 200 ns of
340 simulation, we observed that all three mutants altered the helix's folding to different extents, with
341 a more evident destructuration caused by Ala72Pro and Ala72Val than Phe46Leu (**Figure 4E**).

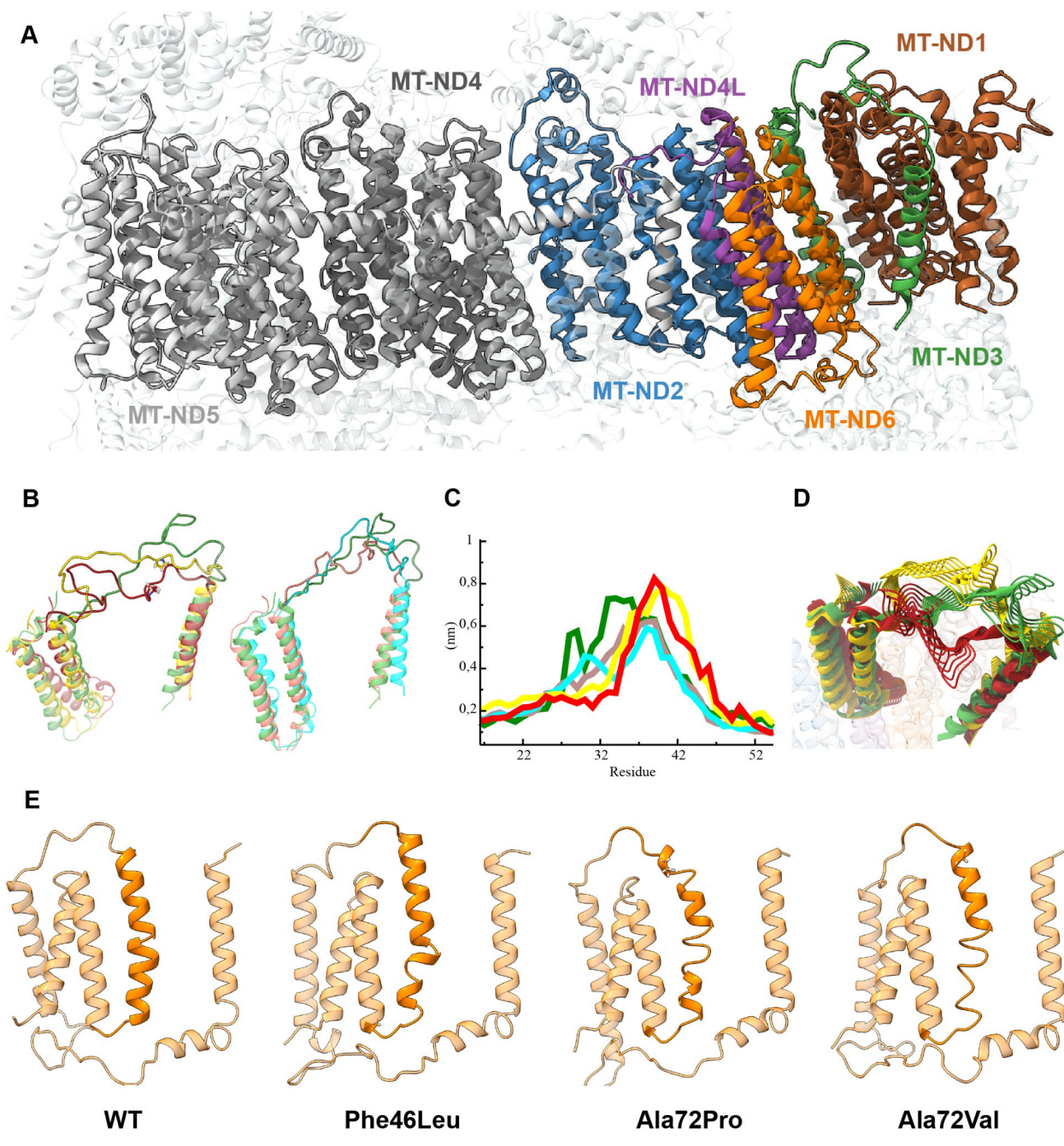
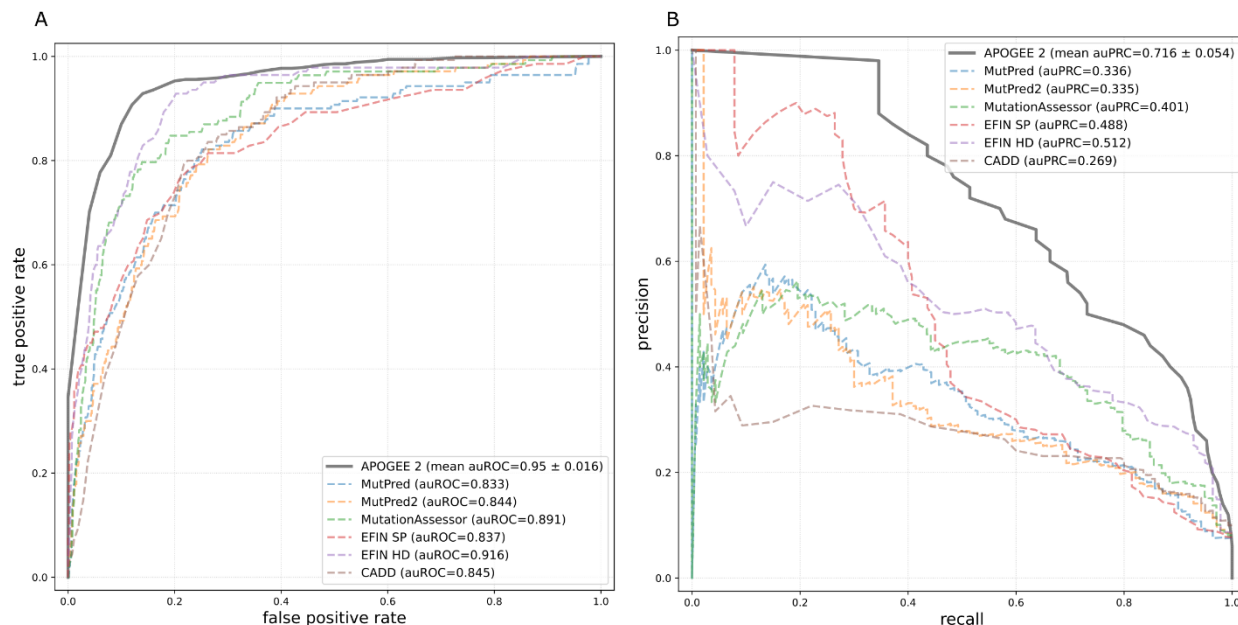


Figure 4. A. Structure of the mtDNA-encoded subunits of the complex I membrane arm. **B.** Average structures of the wild-type, Ser34Pro, and Thr35Pro MT-ND3 protein models (left) and wild-type, Ser34Phe, and Ser34Tyr (right). **C.** RMSF profiles of the heavy atoms of the MT-ND3 loop (residues 24-54) for both wild-type and mutants. **D.** 3D representations of the dynamics of the wild-type, Ser34Pro, and Thr35Pro MT-ND3 protein models. In all subfigures B, C, and D, wild-type is colored green, Ser34Pro is yellow, Thr35Pro is red, Ser34Phe is pink, and Ser34Tyr is cyan. **E.** Average structures of the MT-ND6 protein. TMH3 is highlighted in dark orange.

351 Discussion

352 APOGEE 2 is an ensemble method that addresses the need for a pathogenicity prediction tool
353 with increased accuracy for interpreting missense mtDNA variants. We have shown that it
354 outperforms the former version due to the availability of more mitochondrially-centered features,
355 their manual curation, and the adoption of a more sophisticated ML protocol. Overall, APOGEE
356 2 offers the best performance metrics when compared to other meta-predictors. It is interesting
357 to note, though, that Condel and MtoolBox excel in sensitivity at the expense of their specificity
358 (**Supplementary Table 4**). APOGEE 2 outperforms several other predictors as well, i.e.,
359 MutPred and MutPred2⁵⁰, and MutationAssessor, CADD, and EFIN (**Supplementary Figure**
360 **3**), which were used for APOGEE 2's training.



361
362 **Supplementary Figure 3:** Performance comparison of APOGEE 2 versus other predictors in terms of
363 auROC (A) and auPRC (B). APOGEE 2's performance is reported as the mean ± 95% CIs obtained
364 through cross-validation.
365
366
367 EFIN HD is the only predictor with a higher specificity score. It identifies 1633 of 1734 likely
368 neutral variants versus 1544 which were identified by APOGEE 2. It should be noted, though,

369 that the degrees of certainty of the pathogenic and neutral variants of our training set differ. The
370 pathogenicity of variants is based on the literature. Neutrality is assumed by allelic frequency
371 considerations and available MITOMAP annotations. Given that some variants with literature
372 reports of suspected pathogenicity show frequency levels higher than 0.002% in gnomAD and
373 HelixMTdb, it is also likely that some variants that make up the neutral subset of **Dataset 1** are
374 actually pathogenic. The reverse is not obvious. We have then tested APOGEE 2 and EFIN HD
375 on ClinGen's recently released neutral variants; in general, APOGEE 2 assigned lower
376 pathogenicity scores to ClinGen's neutral variants than EFIN HD did (Wilcoxon signed-rank test
377 preceded by quantile transformation of both scoring systems; the EFIN score has been inverted
378 since it is proportional to the neutrality of the variant; ranks sum = 3236, p-value = 0.003).
379 We have demonstrated that the APOGEE 2 pathogenic scores exhibit significant spatial
380 autocorrelation, suggesting that some protein structural regions may be less tolerant to amino
381 acid changes than others. As a result, APOGEE 2 can predict mitochondrial-specific high and
382 low-risk regions, but it may still be ineffective for variants that have non-local structural effects,
383 particularly if the involved regions are low-confidence/destructured. The flexibility of an MT-ND3
384 loop, for example, seems to be the key feature for evaluating the functionality of Thr35Pro.
385 Thr35Pro and Ser34Pro were shown to change the flexibility of the loop-spanning residues 24–
386 40 more than Ser34Tyr and Ser34Phe, two rare variants with no associated phenotypes and
387 dynamics that were similar to the wild-type protein. The motion of this loop was critical in the
388 establishment of essential links with neighboring subunits, which were broken by Thr35Pro. The
389 m.14538A>G, p.Phe46Leu pathogenic variant is deemed likely-benign by APOGEE 2 because
390 its effect is not localized but instead works to disrupt the nearby TMH3 helix, which in turn plays
391 a crucial role in the Complex I closed conformation.
392 This factor may also have an impact on how missense variants are interpreted in terms of their
393 pathogenic potential when combined with other variants, e.g., synergistic variants, or in the
394 context of particular mtDNA haplogroups ²³. Synergistic variants, in particular, can be

395 challenging to assess as they can be common in control populations and involve poorly
396 conserved residues²⁴. These considerations may explain the fact that only one of the 17
397 missense variants classified as possibly synergistic in MITOMAP is predicted as likely-
398 pathogenic by APOGEE 2, which instead classified the remaining 4 as benign, 9 likely-benign,
399 and 3 VUS (**Supplementary Table 8**).
400 Narrowing the number of VUS variants and, therefore, performance improvements are possible
401 by adding more accurate structural features to variants and accounting for their epistatic
402 interactions, still considering that the growth and curation level alone of the true positive
403 MITOMAP variants in the past fourteen years contributed to a smaller and smaller monotonic
404 increase in the APOGEE 2 performance. Molecular dynamics simulations of a significantly high
405 number of variants that may, even if distantly, alter the functional structure of critical
406 components of the mitochondrial proteins or cooperate with other variants to cause a significant
407 respiratory-chain deficiency might contribute in this direction. A pilot project has already started,
408 and preliminary results are available on MitImpact's website.
409 To facilitate use of the APOGEE 2 scoring and pathogenicity probabilities by clinicians and
410 researchers, we have pre-computed these calculations for all missense variants and made them
411 available in MitImpact through its web interface and as a flat file.
412

413 Methods

414 Datasets

415 Four disjoint sets of variants were used in this work. **Dataset 1** comprises 1874 non-
416 synonymous mtDNA variants, divided into 1734 deemed benign and 140 pathogenic variants
417 (**Supplementary Table 5**). The former set was obtained from MITOMAP's "general" variants

418 (accessed on April 20, 2021), which were purged of overlapping MITOMAP's "disease" variants
419 and variants with ClinGen's pathogenic criteria code "PM2." The pathogenic set was made up of
420 MITOMAP "disease" variants, including 41 *confirmed* and 99 *reported* variants. Overlapping
421 MITOMAP's "general" variants were discarded. Neither set contained any synergistic or
422 conflicting variants. **Dataset 2** was obtained from gnomAD version 3.1.2. It contained 36
423 missense variants not present in the training set, which exhibited allelic frequencies $\geq 0.002\%$
424 both in heteroplasmy and homoplasmy. **Dataset 3** was extracted from HelixMTdb ver.
425 20200327 and filtered as **Dataset 2**. Twelve variants were shared with **Dataset 2** and
426 discarded, and 35 were unique to this dataset. **Dataset 4** fetches variants from the benign/likely-
427 benign variant sets approved by the Mitochondrial Variant Curation Expert Panel (VCEP) of
428 ClinGen (<https://clinicalgenome.org/>) as having met the following criteria for mtDNA variants ¹⁰:
429 Benign variants in the set had allele frequencies $> 1\%$ ("BA1") in either MITOMAP, gnomAD, or
430 HelixMTdb and without disease reports or negative in-silico predictors; likely benign variants in
431 the set had allele frequencies of 0.5%-1% ("BS1") in MITOMAP, gnomAD, or HelixMTdb and
432 without disease reports or negative in-silico predictors, and additionally had either a supporting
433 in-silico tool score for benignity or a resulting synonymous amino acid change. All other variants
434 meeting the allele frequency cutoffs but with possible disease associations are referred to the
435 ClinGen mitochondrial VCEP for individual curation. The current set of benign/likely-benign
436 variants meeting the ClinGen criteria is available at <https://mitomap.org/MITOMAP/Benign> and
437 was accessed for this study on September 7, 2022, and released while **Dataset 1** was already
438 made up. We gathered 135 neutral missense variants in total, dropped 8 VUS variants, and
439 found that 97 of them overlapped **Dataset 1**. **Datasets 2, 3, and 4** were used to evaluate the
440 specificity of the APOGEE 2 predictions (**Supplementary Table 7**).

441 Features

442 APOGEE 2 was trained on three classes of information: evolution, pathogenicity predictions,
443 and protein structural features.

444 **Evolution:** PhyloP and PhastCons conservation scores on 100 vertebrate species were
445 obtained from the UCSC Table Browser. Empirical substitution scores were obtained from the
446 MtMam rate matrix, built on 12 proteins, i.e., ATP6, ATP8, COX1, COX2, COX3, CYBB, ND1,
447 ND2, ND3, ND4, ND4L, and ND5, which are located on the heavy strand of the mtDNA (3331
448 sites)²⁵. Data are from 20 species of mammals and three close outgroups, i.e., Wallaroo,
449 Opossum, and Platypus. The rate matrix was downloaded from [https://github.com/abacus-](https://github.com/abacus-gene/paml/blob/master/dat/mtmam.dat)
450 [gene/paml/blob/master/dat/mtmam.dat](https://github.com/abacus-gene/paml/blob/master/dat/mtmam.dat).

451 **Pathogenicity predictors:** Pathogenicity scores were retrieved for the following software
452 packages: PolyPhen2²⁶, SIFT²⁷, fathmm²⁸, PROVEAN²⁹, MutationAssessor³⁰, EFIN³¹, CADD³²,
453 PANTHER³³, PhD-SNP³⁴, SNAP³⁵, and MutationTaster³⁶.

454 **Structural features:** The 3D structures of the 13 proteins were retrieved from the RCSB Protein
455 Data Bank (PDB) with the following IDs: 5xtc for the Respiratory Complex I (s, i, j, r, k, l, and m
456 chains for MT-ND1, MT-ND2, MT-ND3, MT-ND4, MT-ND4L, MT-ND5, and MT-ND6,
457 respectively); 5z62 for the Cytochrome C Oxidase (chain A for MT-CO1, chain B for MT-CO2,
458 and chain C for MT-CO3); 5xte for the Respiratory Complex III (chains J and V for Cytochrome
459 b). Since MT-ATP6 and MT-ATP8 were not associated with any resolved X-ray structure, their
460 predicted structures were downloaded from the AlphaFold2³⁷ Protein Structure Database³⁸.
461 The five PDB files were placed on the bisector of a 3D space and spaced $3d$ apart, where $d =$
462 20Å. The total energy variation ($\Delta\Delta G$, K_{cal/mol}) eventually caused by any possible non-
463 synonymous amino acid change was calculated as follows. The structures/models described
464 above were first repaired (FoldX's module *RepairPDB*) and then mutated (*PositionScan*),
465 considering all possible amino acid changes causing missense variations. Each mutant was

466 analyzed energetically using FoldX ver. 5.0³⁹ in comparison with the native structure. FoldX
467 was run with default parameters.

468 All these features except for $\Delta\Delta G$ values, mtMam, and the spatial coordinates of amino acids,
469 were pre-calculated and made available in MitImpact ver. 3.0.6⁴⁰.

470

471 Machine learning workflow

472 The overall learning procedure consists of a double cross-validation procedure that nests an
473 optimization procedure of the best parameter combinations (hyperparameters) of each
474 implemented machine-learning (ML) algorithm under a model selection procedure. The workflow
475 was implemented in Python and made available at <https://github.com/mazzalab/playgrounds> as
476 a Colab notebook.

477 In particular, for each ML algorithm, the whole dataset was primarily split into training and test
478 sets by a stratified 20-fold cross-validation (CV) procedure, implemented in Python's *scikit-*
479 *learn*'s *StratifiedKFold*, and repeated five times. Then, for each unique group, we took it as a
480 holdout and used the remaining groups (19) as a training data set. Each group was guaranteed
481 to maintain the original pathogenic/neutral variant ratio. Then, each training set was
482 progressively subjected to three preprocessing steps: *scaling*, *imputation* of missing values, and
483 *feature selection*.

484 Data preprocessing

485 Values were scaled using the Python *scikit-learn*'s *StandardScaler* module to zero mean and
486 unit variance. The scaler was trained on the training-set features and then used to transform
487 both the training and test sets' values (**Figure 5A**). Pairwise correlations between the scaled
488 values to zero mean and unit variance of non-positional features, namely those not directly

489 involving the genomic or amino acidic positions of variants, for all possible mitochondrial
490 missense variants were obtained using Pearson correlation coefficient. Then, we imputed
491 missing values, as explained in the section below. Finally, a supervised feature selection step
492 was implemented using a Decision Tree classifier (*DecisionTreeClassifier scikit-learn* module)
493 to assess the relative information gain associated with a feature and hence its contribution to
494 the overall decision process. The features that explained less than 1% of the total information
495 gain were dropped. This step was performed on the training set only. Then, the dropped
496 features were removed from the training and test sets (**Figure 5C**).

497 Imputer selection

498 The whole MitImpact content, made up of 22,316 variants regardless of their label (neutral or
499 pathogenic) and excluding the variants in **Dataset 1**, was split into 20 folds. Each fold was
500 iteratively chosen as test- and the remaining 19 as training-variants for each of the following five
501 imputation methods. We implemented two simple interpolation methods based on the mean and
502 median values of the features to be imputed, respectively; a k-Nearest Neighbors imputer
503 (`sklearn.impute.KNNImputer`, $k = 5$); two iterative imputers (`sklearn.impute.IterativeImputer`)
504 based respectively on Bayesian ridge linear regression (`sklearn.linear_model.BayesianRidge`)
505 and Random Forest regression (`sklearn.ensemble.RandomForestRegressor`). Once fitted any of
506 these imputers, we have generated twelve $N \times M$ matrices of probability estimates for each test
507 set by sampling from a uniform distribution in the range $[0, 1]$, where N and M are, respectively,
508 the numbers of variants (rows) and features (columns), and multiplying its values by one of the
509 twelve values in the range 0.25 - 3.00, by a step of 0.25. Therefore, we added a missing value
510 whenever any resulting number lower than the a priori probability of a missing value
511 (precalculated for each feature and made available in **Supplementary Table 9**) appeared in the
512 same position of the matrix. The metric we used to identify the best imputer for this study was
513 the Normalized Root Mean Squared Error (NRMSD) defined as $E[X_{true} - X_{imp}]^2 / V[X_{true}]$,

514 where E and V are respectively the expected value and the variance, X_{true} is the true value, and
515 X_{imp} is the imputed value.

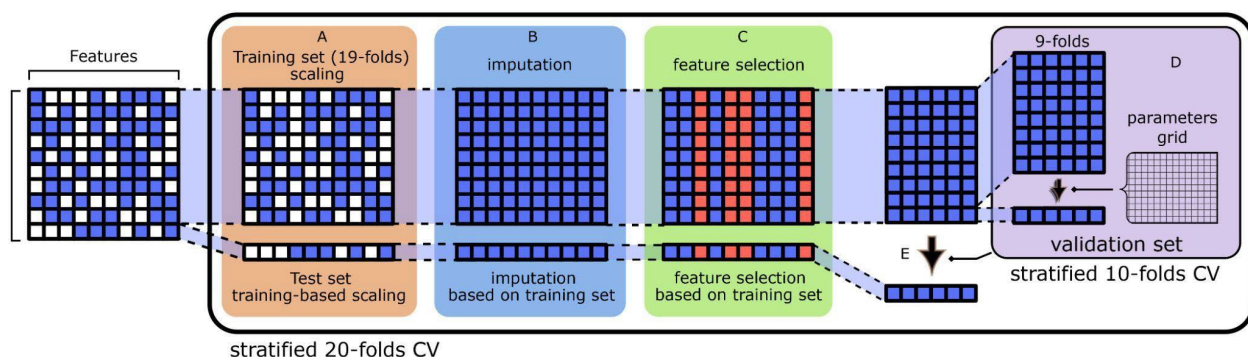
516 Grid-Search cross-validation

517 We performed an exhaustive search over the parameters (or *hyperparameters*) of the tested ML
518 methods using a stratified 10-fold Grid Search CV applied to a pre-computed and method-
519 specific parameter grid (*GridSearchCV* module). The parameter grids for all methods are
520 available in **Supplementary Table 3**. The preprocessed training set was further split into a 9-
521 fold training set and a 1-fold test set. The Grid Search procedure was run for each CV iteration,
522 for a total of $gs = 10 \times d$ times, where d is the number of hyperparameter combinations
523 explored. An ML method was trained and then tested on the 1-fold test set for each combination
524 (**Figure 5D**). The area under the precision-recall curve (auPRC) and under the receiver
525 operating characteristic (auROC) curve metrics were evaluated to assess performance.

526 Model training and testing

527 Each classifier was trained on the 19-fold training set using the best hyperparameter
528 combination found by the Grid-Search loop and then tested on the relative 1-fold test set, which
529 was not involved in the training or tuning phases (**Figure 5E**). The best classifier exhibited a
530 superior average auROC over the five replicas of the overall 20-fold CV process. Then, the total
531 number of iterations performed for each ML method was $100 \times (gs + 1)$.

532



533

534 **Figure 5:** ML pipeline including data preprocessing, i.e., scaling (A), imputation of missing values (B), and
535 feature selection (C), model tuning by 10-folds Grid Search CV (D), training of any ML method with the
536 best hyperparameter combination obtained in D and testing (E).

537

538

539 Finally, we trained a model of the best method on the entire **Dataset 1**, using the best
540 hyperparameters found through the GridSearch CV procedure, and scored all possible non-
541 synonymous mtDNA variants.

542 **ML classifiers**

543 The workflow described above was run with several ML classifiers. Most of them were
544 implemented in the *scikit-learn* Python library.

545 **Support Vector Machine (SVM) with radial basis functions (RBF) kernel.** We implemented
546 the *SVC* module of *scikit-learn*. It attempts to maximize the distance between two groups by
547 minimizing the hinge loss function. The loss function was kept balanced by adjusting the class
548 weights depending on their frequencies in the training set. The method was set to use a Radial
549 Basis Function (*rbf*) as a kernel and L2 as the regularization term. The *rbf* function, defined as
550 $K(x_1, x_2) = e^{(-\gamma ||x_1 - x_2||^2)}$, depends on a parameter γ , which is the inverse of the standard
551 deviation of the *rbf* kernel and represents the influence of each single sample in the learning
552 process, while L2 is controlled by a parameter C , which is inversely proportional to the
553 regularization strength. Both parameters were optimized by Grid-Search.

554 **Gaussian Naive-Bayes (GNB) Balanced Bagging.** This is a probabilistic classifier that uses a
555 Gaussian Naive-Bayes (GNB) model as the base learner for a Bootstrap Aggregation (Bagging)
556 classifier. This approach is typically used to improve the performance of a “weak-learner” (such
557 as the GNB) and reduce overfitting. To tackle the problem of class imbalance in our training set,
558 we resorted to the Balance Bagging classifier implemented by the *imbalanced-learn* package of
559 *scikit-learn*. We have also bootstrapped the features (without replacement) for each base-
560 learner training in an attempt to reduce overfitting. The Grid-Search-based optimization step

561 was applied to i) the ratio of the bootstrapped samples over the total samples; ii) the ratio of the
562 bootstrapped features over the total number of features; and iii) the GNB variance smoothing
563 (more details in the *scikit-learn* documentation).

564 **K-Nearest Neighbors (KNN) Balanced Bagging.** 200 KNN classifiers were used as base
565 learners for a Balanced Bagging classifier with the aim of reducing the risk of overfitting and
566 balancing the pathogenic and neutral classes during the training phase. As in the previous case,
567 the Grid-Search optimization step was used to find the i) ratio of the bootstrapped samples over
568 the total samples, and ii) the ratio of the bootstrapped features over the total number of features.
569 Here, another 2 hyperparameters were subjected to optimization: the number of “neighbors” to
570 consider and the “weight” of each neighbor, which can be considered uniform or the inverse of
571 their distances.

572 **Balanced Random Forest (RF).** This variation of the classical RF classifier is available from
573 *imbalanced-learn* as the *BalancedRandomForestClassifier* module. It is an ensemble method
574 where each tree in a forest will be provided with a balanced bootstrap sample for tree learning.
575 Grid-Search was used to tune i) the trees' maximum depth, ii) the number of random features to
576 consider for each node split, iii) the minimum number of samples required to split a node, and
577 iv) the minimum number of samples that a node requires to be considered a leaf node.

578 **K-Nearest Neighbors (KNN) Bagging balanced through RUS and SMOTE.** We used a
579 synthetic minority over-sampling technique available from the *imbalanced-learn* package and
580 called SMOTE⁴¹ to solve the classification imbalance by generating synthetic samples in the
581 pathogenic class of variants. We combined SMOTE with the randomly under-sampling
582 technique (RUS) according to the following four steps: i) training samples are bootstrapped with
583 replacement, preserving the original training-set size; ii) RUS undersamples the majority class
584 (neutral variants) to partially decrease the imbalance; iii) then, SMOTE is used to generate
585 synthetic minority samples to perfectly balance the base-learner training-set; iv) finally, the
586 base-learner is fitted. Following this procedure, we implemented KNN_RusSmote, which uses a

587 KNN classifier as a base learner. We chose to consider five neighbors in the SMOTE algorithm.
588 As for KNN Balanced Bagging, Grid-Search was used to tune i) the number of “neighbors” to
589 consider, ii) the “weight” of each neighbor, iii) the ratio of the bootstrapped features over the
590 total number of features, iv) the ratio of the minority class over the majority class of samples
591 after the RUS step.

592 Scores and pathogenicity probabilities

593 APOGEE 2 scores are decimal values ranging from 0 (benign) to 1 (pathogenic). Extreme
594 values suggest a high level of confidence in the predictions. Scores were computed using the
595 KNN_RusSmote machine learning algorithm, tuned through GS CV and trained on the whole
596 **Dataset 1**. Given that the algorithm is essentially a bagging model, we were able to determine
597 the out-of-bag (OOB) APOGEE 2 score for each variant in the training set. We used the OOB
598 score to infer the conditional APOGEE 2 probability distribution given the pathogenic class ($C =$
599 1); the APOGEE 2 probability distribution given the benign class ($C = 0$), instead, was inferred
600 on the **Dataset 4** (ClinGen’s benign variants) scores, considering the OOB scores whenever
601 they overlapped with **Dataset 1** (training set). The distributions of both classes were
602 approximated by Beta distributions, whose parameters were optimized through the SciPy
603 Python library by minimizing the negative log-likelihood probability. Once inferred the distribution
604 $P(y | C = 0)$ and $P(y | C = 1)$, where y is the APOGEE 2 score, we could compute the posterior
605 probability $P(C = 1 | y)$ using the Bayes theorem: $P(C = 1 | y) = P(y | C = 1)P(C = 1)/P(y)$,
606 where $P(y)$ can be written in the form $P(y) = P(y | C = 1)P(C = 1) + P(y | C = 0)P(C = 0)$. We
607 set the prior probability $P(C = 1) = 0.1$ as in ¹⁷.

608 Misclassification and specificity assessment

609 In order to calculate the per-class misclassification rate on **Dataset 1**, we first divided the
610 APOGEE 2 scores into two classes (pathogenic and benign) based on the median value. Then,
611 we calculated the frequency of incorrectly classified test variants, which are the variants that
612 were disregarded from the model learning and tuning during CV. Based on the distribution of
613 APOGEE 2 scores for all MitImpact variants, the median threshold was recalculated for each
614 test. Using MitImpact's non-benign frequency as the expected frequency for the null hypothesis,
615 we performed a Chi-square test on the alternative hypothesis of having a high frequency of
616 benign variants in **Datasets 2** and **3**. Finally, we compared the average APOGEE 2 scores of
617 the **Dataset 4**'s benign variants with the average APOGEE 2 scores of the **Dataset 1**'s benign
618 variants, using a Mann–Whitney U test; the OOB scores were used for the **Dataset 1**'s benign
619 variants in this test.

620

621 The APOGEE 2's time-dependent learning curve

622 From 2008 through 2020, we fetched the MITOMAP content every two years and generated
623 seven datasets by applying the same criteria we used for **Dataset 1 (Supplementary Table 5)**.
624 We trained APOGEE 2 with these datasets and used the current MITOMAP version (July 2022)
625 for testing the trained models. In particular, we applied a random stratified 5-fold partitioning
626 strategy to the 2022 dataset, obtaining 5 partitions. For each partition, we trained a model on
627 every other training set (2008–2020) and tested it on the partition, making sure to remove every
628 variant already present in the partition from the training sets. The final auROC profile resulted
629 from the average of the auROCs computed on the five different test-partitions. The ML classifier
630 used was still KNN_RusSmote; 10-fold Grid-Search CV has been performed on each training-
631 set.

632

633 **Positionality and impact of variants on the protein structure**

634 **Spatial autocorrelation of the APOGEE 2 scores**

635 Moran's index was used to measure the spatial autocorrelation of the predicted APOGEE 2

636 scores. It is defined as

637

$$I = \frac{N}{\sum_{i=1}^N \sum_{j=1}^N w_{ij}} \frac{\sum_{i=1}^N \sum_{j=1}^N w_{ij}(y_i - \bar{y})(y_j - \bar{y})}{\sum_{i=1}^N (y_i - \bar{y})^2},$$

638 where N is the number of spatial data points and w_{ij} a weight matrix that measures the
639 closeness of each residue in a pair. It ranges from -1 to +1; values significantly lower or higher
640 than the expected value (i.e., $E[I] = \frac{-1}{N-1}$) indicate respectively negative or positive spatial
641 autocorrelation⁴². We used a quadratic distance decay function, i.e., $w_{ij} = d_{ij}^{-2}$, to model the
642 residue closeness in order to prioritize short-range autocorrelation.

643 Calculations were performed separately for each complex, while the APOGEE 2 scores were
644 averaged by residue to have one value for every spatial point. Positional biases were limited by
645 dropping all bagging base estimators, which were trained using at least one spatial feature (i.e.,
646 X, Y, or Z coordinates) from the APOGEE 2 predictions. 84 out of 200 base estimators were
647 selected. This modification required recalculating the APOGEE 2 threshold between benign and
648 pathogenic variants for this analysis. Due to the possibility that the APOGEE 2 scores obtained
649 in this manner had a different distribution than the original one, we determined the pathogenicity
650 threshold for this new distribution using the same formula we described in the "Model training
651 and testing" methods section.

652 The weight matrix was row-normalized and then renormalized to ensure that $\sum_{i=1}^N \sum_{j=1}^N w_{ij} = 1$;
653 the variable of interest, y , i.e., the APOGEE 2 average scores, was also standardized.
654 Consequently $I = Z'WZ$, where Z is the vector of the standardized values of y and W is the

655 normalized weight matrix. P-values were calculated by permuting the APOGEE 2 scores 10,000
656 times and computing the Moran's index for each permutation.

657 Since we were also interested in estimating the autocorrelation effect under a certain cutoff
658 distance r , we performed the same procedure using a different weight matrix, defined as

659
$$w_{ij} = \begin{cases} 1-\varepsilon, & d_{ij} \leq r \\ 0+\varepsilon, & d_{ij} > r, \end{cases}$$

660 where ε is an infinitesimal number (10^{-6}) whose purpose is only to make the weight matrix row-
661 normalizable. We computed the Moran's index using this weight function at multiple cutoff
662 distances, each time estimating a p-value on 1000 permutations.

663 Finally, we implemented a local version of Moran's index, LISA⁴³ or Local Indicators of Spatial
664 Association, to investigate which regions contribute more to the global spatial autocorrelation. It
665 is defined as $l = [l_1, \dots, l_N] = Z \cdot WZ$, where the weight matrix W was introduced above and
666 $\sum_{i=1}^N l_i = I$. High LISA values are assigned to residues contributing the most to the global
667 positive spatial autocorrelation and showing similar APOGEE 2 scores to their neighbors. To
668 confer significance to the results, we permuted the APOGEE 2 scores 1000 times and
669 computed the l vector for each permutation round; then, we calculated a p-value based only on
670 the l_i random distribution of the spatial point i . The False Discovery Rate was controlled using
671 the Benjamini-Hochberg procedure.

672 Molecular Dynamics simulation

673 Molecular Dynamics (MD) simulations were conducted on the human respiratory complex I
674 transmembrane arm (PDB ID: 5xtc, described above). The starting system was refined using
675 MODELLER ver. 9.16⁴⁴ and then mutated *in-silico* using UCSF Chimera ver. 1.16⁴⁵ to
676 introduce S34P, S34Y, S34F, and T35P amino acid variants in MT-ND3 and A72V, A72P, and
677 F46L variants in MT-ND6. Using the Membrane Builder Input Generator of the CHARMM-GUI
678 web toolkit⁴⁶, the seven resulting alternative protein structures were embedded in a lipid bilayer
679 composed of Palmitoyl-2-oleoyl-sn-glycero-3-phosphocholine (POPC), 1-palmitoyl-2-oleoyl-sn-

680 glycero-3-phosphoethanolamine (POPE), and 1,1',2,2'-tetraoleoyl-cardiolipin (TOCL) to mimic
681 the composition of the inner mitochondrial membrane that forms tight interactions with the
682 transmembrane helix of each protein. Then, both the proteins and the lipid bilayer were solvated
683 in a periodic boundary condition box filled with 22.5Å of TIP3P water molecules on either side of
684 the bilayer, and a salt concentration of 0.15 M KCl was added to obtain a neutral simulation
685 system.

686 All generated systems were energy minimized and equilibrated following the CHARMM-GUI's
687 workflow, consisting of i) steepest-descent minimization for 5000 steps; ii) a gradually heating
688 process conducted into a canonical ensemble (NVT) for 250000 steps with a timestep of 1 fs; iii)
689 an isothermal-isobaric ensemble equilibration for 125000 steps with a timestep of 1 fs followed
690 by 750000 steps of an isothermal-isobaric ensemble equilibration every 2 fs. During the
691 equilibration, harmonic restraints were applied to both the heavy protein atoms and the
692 membrane lipid phosphates.

693 Gaussian accelerated Molecular Dynamics (GaMD)⁴⁷ simulations were performed, starting with
694 a 20 ns short classical MD simulation used to collect potential statistics for calculating the
695 GaMD acceleration parameter, followed by ~80 ns equilibration run. Finally, 200 ns of GaMD
696 simulations were carried out, divided into 10 sequential production steps. Three replicas of the
697 simulation of the wild-type and each mutant system were performed using *Amber20*⁴⁸. Every
698 GaMD simulation was performed at the "dual-boost" level, with one boost applied to the total
699 potential energetic term and the other to the dihedral energetic term. For both the dihedral and
700 the total potential energetic terms, 12.0 kcal/mol was chosen as the upper limit of the boost
701 potential SD, σ_0 . The code for the entire simulation workflow is provided in **Supplementary File**
702 **1**.

703 Analysis of simulated trajectories

704 *AmberTools21* was used to calculate the Root-Mean-Square Fluctuation (RMSF), which
705 measures the time deviation of the positions of the atomic coordinates of the alpha carbons of
706 each residue and those of the reference starting structure. The *GetContacts*
707 (<https://getcontacts.github.io>) tool was used to compute all the atomic interactions and contacts
708 established in each time frame of the simulated trajectories. Secondary structures were
709 computed using the DSSP module of the MDTraj⁴⁹ tool for each simulation frame. The DSSP
710 assignments were calculated using the 8-category schemes: H=α helix, B=residue in isolated
711 beta-bridge, E=extended strand, participating in beta ladder, G=3-helix (3/10 helix), I=5-helix (π
712 helix), T=hydrogen bonded turn, S=bend, – =unclassified. 3D images and motions were
713 generated using UCSF Chimera.

714

715 Data Availability

716 The datasets supporting the conclusions of this article are included within the article and its
717 additional files. The MitImpact database, together with the APOGEE 2 probabilities/classes of
718 pathogenicity, can be freely downloaded from <http://mitimpact.css-mendel.it>. Datasets 2 and 3
719 are available from <https://gnomad.broadinstitute.org/> and
720 <https://www.helix.com/pages/mitochondrial-variant-database>, respectively. Dataset 4 is
721 available from MITOMAP at <https://mitomap.org/MITOMAP/Benign>.

722 Code Availability

723

724 The complete molecular dynamics simulation protocol is available as Supplementary File 1. The
725 APOGEE 2 machine-learning workflow is available from
726 <https://github.com/mazzalab/playgrounds> and is freely runnable as a Colab notebook.
727

728

References

- 729 1. Muller, H. J. The relation of recombination to mutational advance. *Mutat. Res.* **106**, 2–9
730 (1964).
- 731 2. Johnston, I. G. et al. Stochastic modelling, Bayesian inference, and new in vivo
732 measurements elucidate the debated mtDNA bottleneck mechanism. *eLife* **4**, e07464
733 (2015).
- 734 3. Shokolenko, I. N., Wilson, G. L., & Alexeyev, M. F. The "fast" and the "slow" modes of
735 mitochondrial DNA degradation. *Mitochondrial DNA A DNA Mapp. Seq. Anal.* **27**, 490–498
736 (2016).
- 737 4. Allio, R., Donega, S., Galtier, N. & Nabholz, B. Large Variation in the Ratio of Mitochondrial
738 to Nuclear Mutation Rate across Animals: Implications for Genetic Diversity and the Use of
739 Mitochondrial DNA as a Molecular Marker. *Mol. Biol. Evol.* **34**, 2762–2772 (2017).
- 740 5. Szczepanowska, K. & Trifunovic, A. Different faces of mitochondrial DNA mutators.
741 *Biochim. Biophys. Acta* **1847**, 1362–1372 (2015).
- 742 6. Gorman, G. S. et al. Mitochondrial diseases. *Nat. Rev. Dis. Primers.* **2**, 16080 (2016).
- 743 7. Lott, M. T. et al. mtDNA Variation and Analysis Using Mitomap and Mitomaster. *Curr.*
744 *Protoc. Bioinformatics* **44**, 1.23.1–26 (2013).
- 745 8. Laricchia, K. M. et al. Mitochondrial DNA variation across 56,434 individuals in gnomAD.
746 *Genome Res.* **32**, 569–582 (2022).
- 747 9. Bolze, A. et al. A catalog of homoplasmic and heteroplasmic mitochondrial DNA variants in

- 748 humans. Preprint at *bioRxiv* <https://doi.org/10.1101/798264> (2019).
- 749 10. McCormick, E. M. et al. Specifications of the ACMG/AMP standards and guidelines for
750 mitochondrial DNA variant interpretation. *Hum. Mutat.* **41**, 2028–2057 (2020).
- 751 11. Richards, S. et al. Standards and guidelines for the interpretation of sequence variants: a
752 joint consensus recommendation of the American College of Medical Genetics and
753 Genomics and the Association for Molecular Pathology. *Genet. Med.* **17**, 405–424 (2015).
- 754 12. Sonney, S. et al. Predicting the pathogenicity of novel variants in mitochondrial tRNA with
755 MitoTIP. *PLoS Comput. Biol.* **13**, e1005867 (2017).
- 756 13. Preste, R., Vitale, O., Clima, R., Gasparre, G. & Attimonelli, M. HmtVar: a new resource for
757 human mitochondrial variations and pathogenicity data. *Nucleic Acids Res.* **47**, D1202–
758 D1210 (2019).
- 759 14. Castellana, S. et al. High-confidence assessment of functional impact of human
760 mitochondrial non-synonymous genome variations by APOGEE. *PLoS Comput. Biol.* **13**,
761 e1005628 (2017).
- 762 15. Castellana, S. & Mazza, T. Congruency in the prediction of pathogenic missense mutations:
763 state-of-the-art web-based tools. *Brief. Bioinform.* **14**, 448–459 (2013).
- 764 16. Niroula, A. & Vihinen, M. How good are pathogenicity predictors in detecting benign
765 variants? *PLoS Comput. Biol.* **15**, e1006481 (2019).
- 766 17. Tavtigian, S. V. et al. Modeling the ACMG/AMP variant classification guidelines as a
767 Bayesian classification framework. *Genet. Med.* **20**, 1054–1060 (2018).
- 768 18. Marsh, L. Spatial Autocorrelation of Amino Acid Replacement Rates in the Vasopressin
769 Receptor Family. *J. Mol. Evol.* **68**, 28–39 (2009).
- 770 19. Burger, N. et al. ND3 Cys39 in complex I is exposed during mitochondrial respiration. *Cell*
771 *Chem. Biol.* **29**, 636–649.e14 (2022)
- 772 20. Peverelli, L. et al. Leber's Hereditary Optic Neuropathy: A Report on Novel mtDNA
773 Pathogenic Variants. *Front. Neurol.* **12**, 657317 (2021).

- 774 21. Letts, J. A., Fiedorczuk, K., Degliesposti, G., Skehel, M. & Sazanov, L. A. Structures of
775 Respiratory Supercomplex I+III Reveal Functional and Conformational Crosstalk. *Mol. Cell*
776 **75**, 1131–1146.e6 (2019).
- 777 22. Vercellino, I. & Sazanov, L. A. The assembly, regulation and function of the mitochondrial
778 respiratory chain. *Nat. Rev. Mol. Cell Biol.* **23**, 141–161 (2022).
- 779 23. Hudson, G. et al. Clinical expression of Leber hereditary optic neuropathy is affected by the
780 mitochondrial DNA-haplogroup background. *Am. J. Hum. Genet.* **81**, 228–233 (2007).
- 781 24. Caporali, L. et al. Peculiar combinations of individually non-pathogenic missense
782 mitochondrial DNA variants cause low penetrance Leber's hereditary optic neuropathy.
783 *PLoS Genet.* **14**, e1007210 (2018).
- 784 25. Cao, Y. et al. Conflict among individual mitochondrial proteins in resolving the phylogeny of
785 eutherian orders. *J. Mol. Evol.* **47**, 307–322 (1998).
- 786 26. Adzhubei, I. A. et al. A method and server for predicting damaging missense mutations.
787 *Nat. Methods* **7**, 248–249 (2010).
- 788 27. Ng, P. C. & Henikoff, S. SIFT: Predicting amino acid changes that affect protein function.
789 *Nucleic Acids Res.* **31**, 3812–3814 (2003).
- 790 28. Shihab, H. A. et al. Predicting the functional, molecular, and phenotypic consequences of
791 amino acid substitutions using hidden Markov models. *Hum. Mutat.* **34**, 57–65 (2013).
- 792 29. Choi, Y. & Chan, A. P. PROVEAN web server: a tool to predict the functional effect of
793 amino acid substitutions and indels. *Bioinformatics* **31**, 2745–2747 (2015).
- 794 30. Reva, B., Antipin, Y. & Sander, C. Predicting the functional impact of protein mutations:
795 application to cancer genomics. *Nucleic Acids Res.* **39**, e118 (2011).
- 796 31. Zeng, S., Yang, J., Chung, B. H.-Y., Lau, Y. & Yang, W. EFIN: predicting the functional
797 impact of nonsynonymous single nucleotide polymorphisms in human genome. *BMC*
798 *Genomics* **15**, 455 (2014).
- 799 32. Rentzsch, P., Witten, D., Cooper, G. M., Shendure, J. & Kircher, M. CADD: predicting the

- 800 deleteriousness of variants throughout the human genome. *Nucleic Acids Res.* **47**, D886–
801 D894 (2019).
- 802 33. Thomas, P. D. et al. PANTHER: a library of protein families and subfamilies indexed by
803 function. *Genome Res.* **13**, 2129–2141 (2003).
- 804 34. Capriotti, E. & Fariselli, P. PhD-SNPg: a webserver and lightweight tool for scoring single
805 nucleotide variants. *Nucleic Acids Res.* **45**, W247–W252 (2017).
- 806 35. Johnson, A. D. et al. SNAP: a web-based tool for identification and annotation of proxy
807 SNPs using HapMap. *Bioinformatics* **24**, 2938–2939 (2008).
- 808 36. Schwarz, J. M., Cooper, D. N., Schuelke, M. & Seelow, D. MutationTaster2: mutation
809 prediction for the deep-sequencing age. *Nat. Methods* **11**, 361–362 (2014).
- 810 37. Jumper, J. et al. Highly accurate protein structure prediction with AlphaFold. *Nature* **596**,
811 583–589 (2021).
- 812 38. Tunyasuvunakool, K. et al. Highly accurate protein structure prediction for the human
813 proteome. *Nature* **596**, 590–596 (2021).
- 814 39. Delgado, J., Radusky, L. G., Cianferoni, D. & Serrano, L. FoldX 5.0: working with RNA,
815 small molecules and a new graphical interface. *Bioinformatics* **35**, 4168–4169 (2019).
- 816 40. Castellana, S., Rónai, J. & Mazza, T. MitImpact: an Exhaustive Collection of Pre-computed
817 Pathogenicity Predictions of Human Mitochondrial Non-synonymous Variants. *Hum. Mutat.*
818 **36**, E2413–E2422 (2015).
- 819 41. Chawla, N. V., Bowyer, K. W., Hall, L. O. & Kegelmeyer, W. P. SMOTE: Synthetic Minority
820 Over-sampling Technique. *J. Artif. Intell. Res.* **16**, 321–357 (2002).
- 821 42. Sokal, R. R. & Oden, N. L. Spatial autocorrelation in biology: 1. Methodology. *Biol. J. Linn.
822 Soc. Lond.* **10**, 199–228 (2008).
- 823 43. Chen, Y. New Approaches for Calculating Moran's Index of Spatial Autocorrelation. *PLoS
824 One* **8**, e68336 (2013).
- 825 44. Eswar, N. et al. Comparative protein structure modeling using Modeller. *Curr. Protoc.*

- 826 *Bioinformatics Chapter 5*, Unit–5.6 (2006).
- 827 45. Pettersen, E. F. et al. UCSF Chimera--a visualization system for exploratory research and
828 analysis. *J. Comput. Chem.* **25**, 1605–1612 (2004).
- 829 46. Wu, E. L. et al. CHARMM-GUI Membrane Builder toward realistic biological membrane
830 simulations. *J. Comput. Chem.* **35**, 1997–2004 (2014).
- 831 47. Wang, J. et al. Gaussian accelerated molecular dynamics (GaMD): principles and
832 applications. *Wiley Interdiscip. Rev. Comput. Mol. Sci.* **11**, e1521 (2021).
- 833 48. Case, D. A. et al. The Amber biomolecular simulation programs. *J. Comput. Chem.* **26**,
834 1668–1688 (2005).
- 835 49. McGibbon, R. T. et al. MDTraj: A Modern Open Library for the Analysis of Molecular
836 Dynamics Trajectories. *Biophys. J.* **109**, 1528–1532 (2015).
- 837 50. Pejaver V. et al. Inferring the molecular and phenotypic impact of amino acid variants with
838 MutPred2. *Nat. Commun.* **11**, 5918 (2020).

839

840 Acknowledgements

841 This research was funded by the Italian Ministry of Health (Ricerca Corrente 2020-2022) and
842 the "5x1000" voluntary contributions and supported by NVIDIA Corporation and the Amber
843 team. Additional support came from National Institutes of Health grants NS021328, MH108592,
844 OD010944, and CA259635 awarded to D.C. Wallace.

845 Author contributions

846 SDB designed, implemented, and benchmarked APOGEE 2 with the help of LP; FP and TB
847 performed molecular dynamics simulations; SC handled APOGEE 2 integration into MitImpact;
848 AG contributed with data curation; NL and AN validated APOGEE 2 and helped make it

849 available as a public notebook; VP and ML provided temporal MITOMAP data and contributed
850 to the definition of variant pathogenicity criteria; TM conceived the project; TM and VC
851 supervised, respectively, the computational and genetic aspects of the work with the assistance
852 of MC, ALV, and DCW. TM wrote the paper, with contributions from all authors.

853 **Competing interests**

854 All authors declare that the research was conducted in the absence of any commercial or
855 financial relationships that could be construed as a potential conflict of interest.

856

857 Figures

858 **Figure 1:** **A.** Counts (top) of reported and confirmed missense variants for all mtDNA protein-coding
859 genes and their frequency (bottom) calculated on each gene length. **B.** Common missense variants
860 between HelixMTdb, gnomAD, and MITOMAP's confirmed and reported variants. **C.** Distribution of
861 heteroplasmic (gnomAD, $n = 164$, HelixMTdb, $n = 204$) and homoplasmic (gnomAD, $n = 187$, HelixMTdb,
862 $n = 198$) reported variants in gnomAD (left) and HelixMTdb (right) based on their AF. Dashed lines
863 represent the 0.002%, 0.5%, and 1% AF thresholds. Error bars represent the 95% CIs around the median
864 values. Red dots are outlier variants by AF.

865 **Figure 2:** **A.** Average test auPRC values of the selected ML methods, calculated during the training
866 phase. Support Vector Machine classifier with radial basis functions kernel (rbfSVC), Balanced Bagging
867 using Gaussian Naive Bayes (GNB_BalancedBagging) and K-Nearest Neighbors
868 (KNN_BalancedBagging) as base estimators, Balanced Random Forest (BalancedRF), KNN Bagging
869 balanced through RUS and SMOTE techniques (KNN_RusSmote). **B.** Feature importance assessed on
870 the whole Dataset 1; threshold set to 1%. **C.** AuROC values calculated on 118 and 13 neutral and
871 pathogenic test variants for APOGEE versions 1 and 2. **D.** Performance comparison of APOGEE 2 versus
872 other meta-predictors in terms of auROC. APOGEE 2's auROC is reported as the mean \pm 95% CIs
873 obtained through cross-validation. **E.** Time-dependent APOGEE 2's auROC values obtained by predicting
874 MITOMAP 2022 upon training on the 2008-2020 contents; for each year, the sample mean distribution is
875 reported in gray.

876 **Figure 3:** **A.** Distribution of APOGEE 2 scores. Colors represent classes of pathogenicity: green (benign,
877 probability of pathogenicity ($P \leq 0.001$), light green (likely benign, $0.001 < P \leq 0.1$), yellow (VUS, $0.1 < P$
878 < 0.9), orange (likely pathogenic, $0.9 \leq P < 0.99$), red (pathogenic, $P \geq 0.99$). **B.** Misclassification rate of
879 100 test folds calculated on Dataset 1. **C.** Mitochondrial protein complexes localization on the bisector of
880 a 3D space. Colors have the same meaning as **Figure 3A**. **D.** Global spatial autocorrelation computed at
881 different cutoff distances. Blue circles mark the maximum values for each protein complex. **E.** Low-risk
882 (green) and high-risk (in red) amino acid regions of the mitochondrial Complex I subunits. Highlighted in
883 red, we underline the MITOMAP confirmed variants that localize on TMH3 of MT-ND6 and on the MT-
884 ND3 loop.

885 **Figure 4: A.** Structure of the mtDNA-encoded subunits of the complex I membrane arm. **B.** Average
886 structures of the wild-type, Ser34Pro, and Thr35Pro MT-ND3 protein models (left) and wild-type,
887 Ser34Phe, and Ser34Tyr (right). **C.** RMSF profiles of the heavy atoms of the MT-ND3 loop (residues 24-
888 54) for both wild-type and mutants. **D.** 3D representations of the dynamics of the wild-type, Ser34Pro, and
889 Thr35Pro MT-ND3 protein models. In all subfigures B, C, and D, wild-type is colored green, Ser34Pro is
890 yellow, Thr35Pro is red, Ser34Phe is pink, and Ser34Tyr is cyan. **E.** Average structures of the MT-ND6
891 protein. TMH3 is highlighted in dark orange.

892 **Figure 5:** ML pipeline including data preprocessing, i.e., scaling (A), imputation of missing values (B),
893 and feature selection (C), model tuning by 10-folds Grid Search CV (D), training of any ML method with
894 the best hyperparameter combination obtained in D and testing (E).

895 Supplementary Figures

896 **Supplementary Figure 1:** Matrix of Pearson correlation coefficients calculated on the scaled prediction
897 scores to zero mean and unit variance of non-positional features for all possible mitochondrial missense
898 variants. Axes labels related to pathogenicity predictors are highlighted in bold. **B.** Imputation of missing
899 values with five algorithmic strategies; performance is measured in terms of Normalized Root Mean
900 Squared Error (NRMSE, Y-axis); multipliers of the *a priori* probability of missing values in MitImpact (i.e.,
901 the unitary value) on the X axis (see Methods); both mean errors (lines) and their 95% CI (colored
902 shadows) are reported in the figure.

903 **Supplementary Figure 2: A.** 83 (4.7%) heteroplasmic variants in gnomAD were predicted to be likely
904 pathogenic, and 10 (0.6%) were pathogenic. 71 (4%) and 7 (0.4%) variants exhibited an AF <0.002%,
905 respectively. 19 (0.9%) homoplasmic variants were classified as likely pathogenic and 3 (0.1%) as
906 pathogenic. 11 (0.5%) and 1 (0.05%) variants exhibited an AF <0.002 %, respectively. **B.** 101 (3.3%)
907 HelixMTdb heteroplasmic variants were predicted as likely pathogenic, and 15 (0.5%) were classified as
908 pathogenic. Similarly, 33 (1.1%) homoplasmic variants were defined as likely pathogenic, and 3 (0.1%)
909 were deemed pathogenic. 86 (2.8%) heteroplasmic and 22 (0.8%) homoplasmic likely pathogenic
910 variants exhibited an AF <0.002%; 13 (0.4%) and 2 (0.07%) considering heteroplasmic and homoplasmic

911 pathogenic variants, respectively. Both panels represent the APOGEE 2 pathogenicity probability values
912 of heteroplasmic (left) and homoplasmic (right) variants on the Y axis and the variant AF on the X axis. A
913 dot is a variant. A dot color represents the pathogenicity level (green = benign, red = pathogenic), as in
914 Figure 3D. The red dashed line marks the 0.002% AF threshold. The blue dashed lines separate likely-
915 benign from VUS (score = 0.2654, probability = 0.1) and VUS from likely-pathogenic (score = 0.7161,
916 probability = 0.9). **C.** Frequency distribution of APOGEE 2 scores of Dataset 1's benign variants (training
917 set) and Dataset 4's variants (ClinGen). Vertical dashed lines mark the average APOGEE 2 scores for
918 both distributions.

919 **Supplementary Figure 3:** Performance comparison of APOGEE 2 versus other predictors in terms of
920 auROC (A) and auPRC (B). APOGEE 2's performance is reported as the mean \pm 95% CIs obtained
921 through cross-validation.

922

923 Supplementary Tables

924 **Supplementary Table 1:** GnomAD variants that are in MITOMAP as confirmed, those with an
925 allele frequency greater than 0.002%, plus three gnomAD variants that were deemed
926 pathogenic by ClinVar (accessed in October 2021). We also reported HelixMTdb variants
927 showing an allele frequency $\geq 0.002\%$ and a confirmed disease status according to MITOMAP.

928 **Supplementary Table 2:** Correlation matrix of the evolution, pathogenicity predictions, and
929 protein structural features used to train APOGEE 2. It includes three evolution measures,
930 fourteen *in silico* pathogenicity predictors, and one protein structural feature. Pearson
931 correlation coefficients are reported.

932 **Supplementary Table 3:** Parameter grids tested through GridSearch CV for all the machine
933 learning methods evaluated in this work. The best parameters found for the selected method
934 are marked in bold.

935 **Supplementary Table 4:** Performance metrics of all the machine learning methods evaluated in
936 this work and performance comparison between APOGEE 2 and other meta-predictors. In the
937 upper table, for each metric, we reported the average performance \pm 95% confidence intervals,
938 calculated on 100 test folds. In the lower table, we reported the average performance metrics for
939 all the meta-predictors compared to APOGEE 2.

940 **Supplementary Table 5:** List of all MitImpact variants annotated and categorized according to
941 APOGEE 2. Variants belonging to the training set (Dataset 1) have been flagged as “P” or “N”
942 referring to pathogenic or deemed benign variants, respectively.

943 **Supplementary Table 6:** List of the most significantly high local spatial autocorrelated amino
944 acids (adjusted LISA permutation p-value <0.01).

945 **Supplementary Table 7:** Datasets 2, 3, and 4 containing benign or likely benign variants, used
946 to evaluate the specificity of the APOGEE2 predictions. Datasets 2 and 3 were retrieved from
947 gnomAD and HelixMTdb, respectively, considering missense variants not included in the
948 training set, showing an allele frequency $\geq 0.002\%$ (according to the source database). Dataset
949 4 was obtained from MITOMAP (<https://mitomap.org/MITOMAP/Benign>, accessed on
950 September 7, 2022) and refers to non-synonymous curated variants not included in the training
951 set and flagged as Benign or Likely-benign.

952 **Supplementary Table 8:** List of possible synergistic variants in MITOMAP. We functionally
953 annotated each variant and reported its classification according to APOGEE 2.

954 **Supplementary Table 9:** Frequency of missing values of APOGEE 2 features in Mitimpact.

955 **Supplementary Table 10:** auROC values calculated on 5 random partitions of the 2022
956 MITOMAP dataset, after training APOGEE 2 on seven MITOMAP sets retrieved from 2008 to
957 2020 every two years.